

# Atomic-level Insights into the Highly Conductive Lithium Thiophosphate Solid Electrolytes with Exceptional Stability Against Lithium Metal

Huseyin Sener Sen<sup>1\*</sup>, Bora Karasulu<sup>1\*</sup>

<sup>1</sup>Department of Chemistry, University of Warwick, Coventry CV4 7AL, U.K.

\*corresponding authors

## Abstract

Despite the wide range of emerging solid electrolytes with promising characteristics, such as high ionic conductivity, the inherent thermodynamic instability against lithium metal remains a significant challenge. We have previously introduced a new family of solid electrolytes based on thiophosphates with inherent stability against metallic Li anode and high conductivity [JACS REF]. In this study, we employ density functional theory (DFT) together with *ab initio* molecular dynamics (AIMD) simulations to investigate the diffusion mechanisms and underlying factors contributing to the high ionic conductivity of these novel Li-P-S ternary electrolytes, including  $\text{Li}_7\text{PS}_2$ ,  $\text{Li}_5\text{PS}$ ,  $\text{Li}_8\text{P}_2\text{S}$ , and  $\text{Li}_{11}\text{P}_3\text{S}$ . Our findings reveal that these materials exhibit ionic conductivities comparable to the well-known superionic conductor,  $\text{Li}_7\text{P}_3\text{S}_{11}$ , positioning them as promising candidates for solid-state battery applications. Additionally, we assess the thermodynamic stability of these ternaries in contact with lithium metal anodes, a critical consideration for practical battery use. Unlike  $\text{Li}_7\text{P}_3\text{S}_{11}$ , which forms a solid-electrolyte interphase, the novel Li-P-S ternaries exhibit remarkable stability against Li metal anode due to their unique  $\text{Li}_2\text{S}$ -like structural framework. The absence of a solid-electrolyte interphase layer is particularly significant, as it eliminates additional resistance at the electrolyte-anode interface, a common challenge in many solid-state battery systems. Our study not only highlights the suitability of these novel ternaries, particularly  $\text{Li}_5\text{PS}$ , as high-performance solid electrolytes but also underscores the importance of structural design in developing next-generation battery materials. The ability of these materials to maintain high ionic conductivity and stability over extended periods makes them ideal candidates for future solid-state lithium batteries, offering a pathway to safer, more efficient, and longer-lasting energy storage solutions.

## 1. Introduction

In recent years, the pursuit of safer and more efficient energy storage systems has prompted the exploration of alternatives to conventional LIBs.<sup>1</sup> Traditional LIBs, fuelled by liquid electrolytes, exhibit inherent challenges related to safety and energy density. Liquid electrolytes are typically composed of organic solvents, such as ethylene carbonate (EC) or dimethyl carbonate (DMC), which are highly flammable. In the event of a short circuit, overheating, or mechanical damage to the battery, these solvents can ignite, leading to fires or explosions.<sup>2,3</sup> Lithium metal has the highest theoretical capacity of any anode material, making it highly desirable for high-energy-density batteries.<sup>4-6</sup> However, to fully exploit this potential, the electrolyte must be stable in contact with lithium metal. Lithium metal is highly reactive, especially when in contact with conventional liquid electrolytes, which can lead to the formation of lithium dendrites.<sup>7-11</sup> These dendrites can grow through the electrolyte and eventually cause short circuits, leading to battery failure, overheating, and potentially fires or explosions. The emergence of solid-

state batteries, with solid-state electrolytes replacing the traditional liquid counterparts, has marked a significant paradigm shift. In theory, a solid electrolyte enables the use of lithium metal anodes, leading to batteries with significantly higher energy densities compared to those using graphite or other anode materials.<sup>5,10,12-15</sup> Therefore, the transition toward all-solid-state batteries (ASSBs) represents a transformative leap forward because it not only potentially allows the use of pure or alloyed lithium anodes, enabling higher capacities, but also holds the promise of mitigating flammability concerns associated with non-aqueous electrolytes.

ASSBs exhibit superiority over conventional LIBs, particularly in high-temperature applications, offering reduced flammability risks and a diminished threat of thermal runaway.<sup>16,17</sup> Furthermore, the absence of bulk polarization effects, as Li<sup>+</sup>-ions exclusively conduct ionic charge, suggests the potential for faster (dis)charging in ASSBs compared to traditional LIBs.<sup>18</sup> Despite these advantages, the commercialization of lithium ASSBs faces challenges, primarily the absence of a highly conductive solid electrolyte (SE) that is stable toward lithium metal and cathode materials, while accommodating mechanical stresses induced during battery cycling, including volume changes in active materials. Dendrite-free plating of lithium metal remains an unresolved issue.

The exploration of promising SEs has witnessed a proliferation of interest in diverse materials. One class, represented by cation-substituted Li<sub>7</sub>La<sub>3</sub>Zr<sub>2</sub>O<sub>12</sub> (LLZO)-derived compounds,<sup>19</sup> offers high ionic conductivity and kinetic stability toward lithium metal but faces challenges related to mechanical stiffness and susceptibility to cracking as well as lithium dendrite formation particularly at high current densities.<sup>18</sup> A second promising class involves materials containing sulphide ions, exhibiting extremely high ionic conductivity and stress accommodation.<sup>20</sup> In these materials, oxide anions are substituted by larger and more polarizable sulphide anions. This results in reduced Li-ion jump barriers which enhances their conductivity enormously.<sup>21</sup> In fact, materials incorporating thiophosphate polyhedra as fundamental units exhibit remarkably high ionic conductivities comparable to those observed in liquid electrolytes. Studying glasses and crystalline phases within the pseudo-binary (Li<sub>2</sub>S)<sub>x</sub>(P<sub>2</sub>S<sub>5</sub>)<sub>1-x</sub> were one of the first attempts to utilize the presence of thiophosphate polyhedra.<sup>22,23</sup> Recent developments have highlighted that doped crystalline derivatives such as Li<sub>10</sub>GeP<sub>2</sub>S<sub>12</sub> (LGPS,  $\sigma = 12 \text{ mS cm}^{-1}$ ),<sup>24</sup> Li<sub>6-x</sub>PS<sub>5-x</sub>ClBr<sub>x</sub> ( $\sigma = 24 \text{ mS cm}^{-1}$ ),<sup>25</sup> and Li<sub>9.54</sub>Si<sub>1.74</sub>P<sub>1.44</sub>S<sub>11.7</sub>Cl<sub>0.3</sub> ( $\sigma = 25 \text{ mS cm}^{-1}$ )<sup>26</sup> are some of the most conductive solid electrolytes (SEs) to date.

More recently, a third class, lithium-rich ternary phosphides emerged as potential SE candidates, featuring phosphide anions (P<sup>3-</sup>) with even greater polarizabilities than sulphide anions. These phases are structured around anionic TtP<sub>4</sub> tetrahedra, where Tt represents elements such as Al, Si, Ge, Ga, or Sn. Notably, Li<sub>9</sub>AlP<sub>4</sub> demonstrates conductivities of up to 3 mS cm<sup>-1</sup> at room temperature.<sup>27-33</sup> Despite their appeal as SEs due to a high number of charge carriers and low density, these materials exhibit sensitivity to oxygen and moisture.

Although the newly introduced solid electrolyte (SE) materials offer several advantages, they share a significant drawback: they are inherently thermodynamically unstable when in contact with lithium metal, as demonstrated for metal/metalloid-containing oxides, sulphides, and thiophosphates.<sup>34-37</sup> For instance, thiophosphates degrade into a mixture of lithium sulphides and phosphides, driven by the reduction of phosphorus ions from a P<sup>5+</sup> oxidation state to P<sup>3-</sup> in Li<sub>3</sub>P. The resulting lithium binary compounds (Li<sub>2</sub>O, Li<sub>2</sub>S, Li<sub>3</sub>P, and LiX, where X represents a halide) are suboptimal as electrolytes, creating a conductivity bottleneck at the SE-lithium metal interface. Additionally, the reduction of other cations in the material may lead to short circuits due to the formation of lithium intermetallics. For example, Ge<sup>4+</sup> in LGPS<sup>38</sup> and

phosphidogermanates can form electronically conductive germanides,<sup>36,37</sup> which pose a risk of further decomposition and short circuits through the creation of mixed ionic-electronic conducting interphases.<sup>38</sup>

Quantum chemical calculations, primarily employing density functional theory (DFT), have been widely used to investigate the structural, electronic, transport, and spectral properties of various Li-ion battery materials, particularly solid-state electrolytes.<sup>39-41</sup> Moreover, DFT is often combined with crystal structure prediction (CSP) approaches, including stochastic methods such as Ab Initio Random Structure Search (AIRSS), evolutionary algorithms like the genetic algorithm (GA) and USPEX, and particle-swarm optimization methods such as CALYPSO, in the *in silico* discovery of novel functional materials.<sup>42,43</sup> While these tools have been applied to predict chemically-doped thiophosphate electrolytes, such as  $\text{Li}_3\text{Y}(\text{PS}_4)_2$ <sup>44</sup> and  $\text{Li}_x(\text{PS}_4)_y\text{X}_z$  ( $\text{X} = \text{Cl}, \text{Br}, \text{I}$ ),<sup>45</sup> the pure Li-P-S phase diagram has largely remained unexplored, with the exception of individual studies focusing exclusively on a few  $\text{Li}_2\text{S}-\text{P}_2\text{S}_5$  phases.<sup>46</sup>

Despite the wide range of emerging SEs with promising characteristics, the inherent thermodynamic instability against lithium metal remains a significant challenge. Addressing the need for a highly  $\text{Li}^+$ -ion conductive SE that is thermodynamically stable against lithium metal demands a comprehensive approach that includes the careful consideration of structural and thermodynamic characteristics, as well as the synthesis methodology. While defect engineering, such as introducing chemical dopants through ball milling, presents one strategy to achieve high conductivity, we propose a more systematic, three-step approach that offers greater efficiency in terms of both time and cost. The first step involves computationally identifying the most promising compositions through high-throughput crystal structure predictions, followed by their synthesis via solid-state methods like ball milling. The second step focuses on investigating the thermodynamic stability of these solid electrolytes in contact with lithium metal through detailed computational studies, enabling the identification and resolution of any stability issues before moving toward the production and commercialization phase—the final step in the process.

In our previous work,<sup>47</sup> we successfully demonstrated the first step by exploring the Li-P-S ternary phase space, employing a combination of high-throughput crystal structure predictions and solid-state synthesis (via ball milling) to isolate the most promising compositions, particularly those within the  $\text{Li}_3\text{P}-\text{Li}_2\text{S}$  tie line. We conducted a systematic characterization of the structural properties and Li-ion mobility of these materials using techniques such as X-ray and neutron diffraction, solid-state nuclear magnetic resonance spectroscopy (relaxometry), and electrochemical impedance spectroscopy. This led to the identification of several  $\text{Li}_3\text{P}-\text{Li}_2\text{S}$  metastable solid solutions, where the phases adopted a fluorite ( $\text{Li}_2\text{S}$ ) structure with phosphorus substituting for sulphur and extra  $\text{Li}^+$ -ions occupying octahedral voids, thus enhancing ionic transport. The combined analysis of experimental data and quantum-chemical calculations reveals that four of these new ternary compounds— $\text{Li}_7\text{PS}_2$ ,  $\text{Li}_5\text{PS}$ ,  $\text{Li}_8\text{P}_2\text{S}$ , and  $\text{Li}_{11}\text{P}_3\text{S}$ —not only exhibit high structural stability and ionic conductivity but also possess low activation barriers for  $\text{Li}^+$ -ion transport. As shown in Figure 1, these compounds adopt a  $\text{Li}_2\text{S}$ -like orthorhombic (slightly distorted cubic) structural framework, which suggests potential thermodynamic stability in the presence of lithium metal anodes similar to  $\text{Li}_2\text{S}$ .

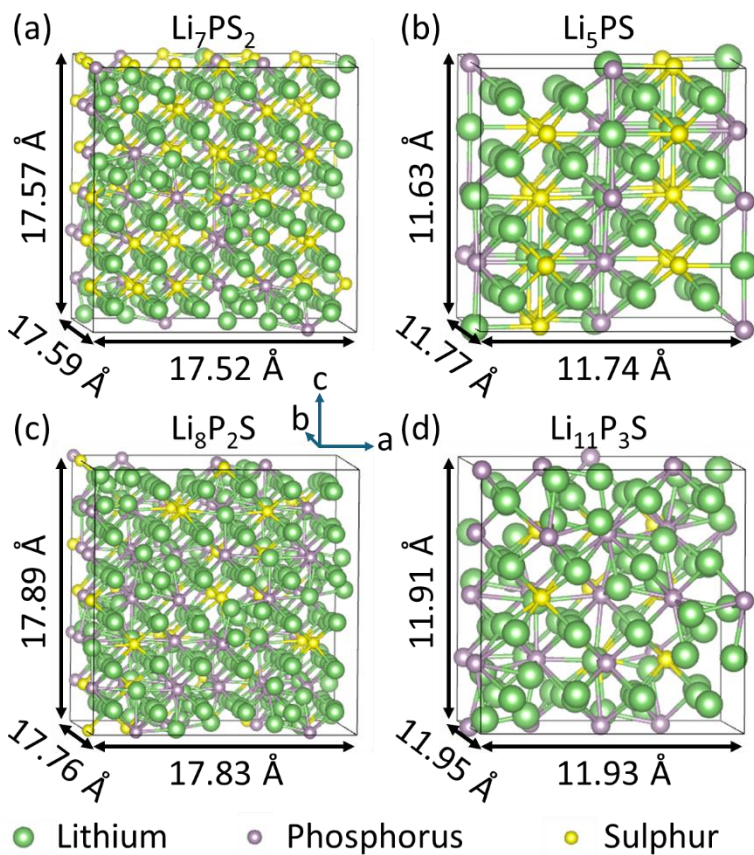


**Figure 1.** Supercells of highly conductive  $\text{Li}_3\text{P}-\text{Li}_2\text{S}$  solid solutions studies in this work; a)  $\text{Li}_7\text{PS}_2$ , b)  $\text{Li}_5\text{PS}$ , c)  $\text{Li}_8\text{P}_2\text{S}$  and d)  $\text{Li}_{11}\text{P}_3\text{S}$ .

In this work, we present the second step of our approach, where we delve into the thermodynamic stability of these four Li-P-S ternaries (see Figure 1) in contact with lithium metal anodes by means of DFT simulations. The article is structured as follows: Section 2 details the methodology and computational approach employed in this study. Section 3 presents the results, beginning with an examination of the bulk structures, followed by an analysis of the surface structures, and concluding with an evaluation of the interfaces and their properties. Finally, Section 4 offers a summary of our findings and outlines the implications for future research.

Our approach represents a significant advancement in the development of solid electrolytes by addressing critical challenges in the field, particularly the instability of SE materials against lithium metal anodes. The novel Li-P-S ternaries we have developed not only demonstrate exceptional stability against lithium anodes—comparable to the highly stable  $\text{Li}_2\text{S}$ —but also exhibit high ionic conductivity without the formation of a solid-electrolyte interphase (SEI), even at elevated temperatures. This absence of SEI formation eliminates internal resistance at the interface, maintaining the high conductivity observed in their bulk structures. Furthermore, our investigation into the underlying mechanisms reveals that phosphorus substitution for sulphur atoms stabilizes extra interstitial sites and coordinates additional lithium atoms, creating new conduction channels that further enhance ionic transport. This dual achievement of stability and conductivity presents a pivotal step forward, offering a robust solution to the

longstanding issues in solid electrolyte design and paving the way for more efficient and safer energy storage systems.

## 2. Computational Methods

### 2.1. INTERFACER code

To investigate the stability against lithium metal anode, formation of SEI layers and improve ionic conductivity at electrolyte-electrode interfaces, we built model interfaces between various Li-P-S structures and lithium metal. To facilitate this, we have developed the *INTERFACER* code,<sup>48</sup> an automated interface generation tool designed to systematically explore various candidate interfaces with minimal strain, starting from predicted bulk structures. By searching through specified Miller indices, INTERFACER identifies energetically-relevant interfaces and, in conjunction with ab initio DFT codes (such as VASP or CASTEP), determines the thermodynamically and mechanically stable configurations. The INTERFACER tool, coded in Python, also integrates parameter setup for ab initio simulations, streamlining the interface optimization process.

### 2.2. VASP parameters for relaxation and ab initio molecular dynamics simulations

Plane-wave DFT electronic structure calculations were performed using the Vienna Ab Initio Simulation Package (v. 6.3),<sup>49–51</sup> which is an implementation of periodic boundary conditions and the pseudopotential approximation. We employed the projector-augmented wave (PAW)<sup>52,53</sup> method jointly with the Perdew-Wang (PW91) version of the Generalized Gradient Approximation (GGA) exchange–correlation potentials.<sup>54</sup> The atomic positions and lattice parameters were fully relaxed using conjugate-gradient method until all forces acting on atoms were smaller than 0.01 eV/Å. The Brillouin zone was sampled using a  $\Gamma$ -centred Monkhorst–Pack (MP) grid with a k-point spacing finer than 0.1 Å<sup>-1</sup>. A cut-off-energy for the planewave basis functions of 520 eV was adopted for the cell and geometry relaxations, while the cut-off was lowered to 400 eV for the *Ab initio* molecular dynamics (AIMD) simulations. For both cell/geometry optimisations and AIMD simulations, the normal accuracy setting (*PREC=Normal*) along with an electronic convergence criterion of 10<sup>-8</sup> eV and a Gaussian smearing factor of 0.1 eV were adopted. To allow for unbiased ionic migration dynamics, no symmetry constraints were applied during the dynamic simulations. AIMD simulations were performed not only to analyse the integrity of the interface, i.e. the SEI formation, but also for estimating the Li-ion conductivity within the Li-P-S ternaries as well as through the interfaces under investigation. For AIMD simulations, we benefitted from the faster implementation in VASP designed for the  $\Gamma$ -only calculations, which proved useful for obtaining numerous adequately long MD trajectories to yield better analysis for diffusivity. All crystal structures were visualized with VESTA<sup>55</sup> and Ovito.<sup>56</sup>

## 3. Results and Discussion

### 3.1. Bulk conductivity comparison: the effect of Phosphorus

Efficient ion transport in solid-state electrolytes is essential for achieving high-performance all-solid-state batteries. Consequently, understanding the diffusion processes and optimising ionic conduction at the nanoscale is a critical focus of contemporary research. In our previous study,<sup>47</sup> we presented both computational and experimental data on the ionic conductivities and activation energies of newly synthesised and other commonly studied Li-P-S ternary systems. Our findings revealed that the new ternaries, particularly Li<sub>7</sub>PS<sub>2</sub>, Li<sub>5</sub>PS, Li<sub>8</sub>P<sub>2</sub>S, and Li<sub>11</sub>P<sub>3</sub>S (see **Figure 1**) exhibited exceptionally high conductivities and low activation energies, comparable to those of the superionic conductor Li<sub>7</sub>P<sub>3</sub>S<sub>11</sub>.

However, we are yet to clarify the underlying reasons for these promising properties as solid electrolytes. While traditional experimental techniques offer valuable insights into macroscopic ionic conductivity, they often lack the resolution necessary to elucidate the atomic-scale mechanisms that govern ion movement, particularly in complex solid-state systems. This is where AIMD simulations become crucial. AIMD enables the detailed investigation of microscopic processes underlying ionic diffusivity, offering an atomistic perspective of ion transport that accounts for the intricate interactions within the material's crystal lattice and electronic structure by simulating ion dynamics within a fully quantum mechanical framework. These simulations are therefore indispensable for the design and optimisation of new solid electrolyte materials with enhanced ionic conductivity, directly influencing the development of next-generation energy storage technologies. In this section, we provide an understanding of the fundamental mechanisms behind the superior diffusion properties of the four newly-developed ternaries mentioned above through AIMD simulations.

The self-diffusivity of ions can be computed from the mean square displacement (MSD) of Li ions during an AIMD simulation. Self-diffusivity, also referred to as the tracer diffusivity ( $D^*$ ), is defined for particle  $i$  as

$$D^* = \lim_{t \rightarrow \infty} \frac{\langle |r_i(t)| \rangle^2}{2dt} \quad (1)$$

where  $d$  is the dimensionality of the diffusion (2 or 3), which we set to 3 in all cases presented here. The MSD of the  $N$  ions within a bulk structure is expressed as:

$$\langle |r(t)| \rangle^2 = \frac{1}{N} \sum_{i=1}^N [r_i(t) - r_i(t=0)]^2. \quad (2)$$

The bulk ionic conductivity of an electrolyte, such as a Li-P-S ternary, can be estimated using the Nernst-Einstein relation,<sup>57</sup> given by:

$$\sigma = \frac{n e^2 Z^2 D H_R}{kT} \quad (3)$$

where  $n$  is the density of diffusing particle,  $e$  is the elementary charge,  $Z$  is the ionic charge,  $k$  is the Boltzmann constant,  $T$  is the temperature and  $D$  is the ion diffusivity, with the Haven Ratio ( $H_R$ ) assumed to be unity (indicating non-correlated ionic motion). Furthermore, the activation energy for a given electrolyte can be determined from an Arrhenius plot, which involves the exponential fit of conductivity versus inverse temperature over a range of temperatures.

**Figure 2a** illustrates the MSD of lithium atoms for bulk-Li-P-S systems at 525 K. The MSD of lithium atoms for  $\text{Li}_2\text{S}$  and  $\text{Li}_3\text{P}$  are not included in this figure due to their almost negligible diffusivities at 525 K. The data reveals that while the lithium mobility in the superionic conductor  $\text{Li}_7\text{P}_3\text{S}_{11}$  is higher than in all other systems, the mobilities in  $\text{Li}_5\text{PS}$  and  $\text{Li}_8\text{P}_2\text{S}$  are quite comparable. Notably, at 100 ps, the MSD for  $\text{Li}_7\text{P}_3\text{S}_{11}$  is only four times larger than that of  $\text{Li}_5\text{PS}$  and  $\text{Li}_8\text{P}_2\text{S}$ . Additionally, all the novel ternary compounds demonstrate significantly higher lithium diffusivity compared to  $\gamma\text{-Li}_3\text{PS}_4$ . These observations underscore the enhanced ionic transport properties of the newly developed ternary systems.

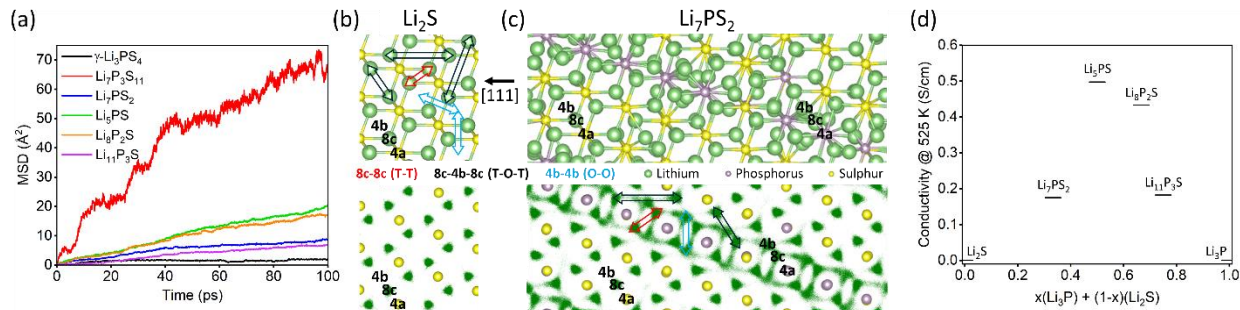


**Figure 2.** Diffusion properties of Li-P-S ternaries. a) MSD of Li-P-S ternaries at 525 K, b) atomistic structure (upper panel) and Li<sup>+</sup>-ion trajectory (lower panel) for bulk Li<sub>2</sub>S at 525 K, c) atomistic structure (upper panel) and Li<sup>+</sup>-ion trajectory (lower panel) for bulk Li<sub>7</sub>PS<sub>2</sub> at 525 K, d) conductivity of Li-P-S systems as a function of Li<sub>2</sub>S-Li<sub>3</sub>P composition ratio at 525 K. The structures are depicted along [111] for ease of comparison to interface structures. The red, black and blue arrows indicate possible diffusion channels for Li<sup>+</sup>-ions along 8c-8c (T-T), 8c-4b-8c (T-O-T) and 4b-4b (O-O), respectively. T/O denotes the tetrahedral/octahedral sites.

From AIMD trajectories, one can also extract the Li-ion transport pathways to elucidate the underlying factors contributing to the enhanced conductivity observed in the new ternary solid solutions. In the Li<sub>2</sub>S structure, lithium atoms occupy the 8c tetrahedral sites, while sulphur atoms reside in the 4a octahedral sites, as illustrated in the upper panel of **Figure 2b**. The 4b octahedral sites are energetically unfavourable for both sulphur and lithium atoms, rendering them unstable and vacant. Three primary ion migration paths can be anticipated in Li<sub>2</sub>S and Li-P-S ternaries: (1) the 8c-8c (T-T) path as shown by red arrows, involving Li hopping between thermodynamically stable tetrahedral sites (i.e., vacancy hopping); (2) the 8c-4b-8c (T-O-T) path as shown by black arrows, where Li jumps between regular and interstitial Li sites; and (3) the 4b-4b (O-O) path as shown by blue arrows, which is only possible for Li-P-S ternaries as Li<sub>2</sub>S lacks interstitials. In the lower panel of **Figure 2b**, we depict the lithium ion trajectory during the whole simulation of 100 ps at 525K with green dots, while the initial positions of sulphur atoms are given as reference. For pristine Li<sub>2</sub>S, AIMD simulations indicate that Li conduction does not occur at 525 K. Li mobility is rather limited and confined to the regular/lattice Li sites, primarily due to the full occupancy of the 8c sites in the model used. Although Li migration through the 8c-8c (T-T) path appears to be the most probable diffusion mechanism, introducing Li lattice vacancies at the 8c sites is not expected to significantly enhance Li mobility at low temperatures.<sup>58,59</sup> Moreover, T-O-T type migration is also absent, consistent with the reported high activation barrier ( $E_a=0.39$  eV).<sup>58</sup> However, at 1075 K, slightly above the previously reported superionic phase transition temperature ( $T \approx 900$  K),<sup>59,60</sup> Li ions begin to diffuse via the T-O-T path, which then becomes the predominant mode of conduction.

Next, we investigate the ionic conduction in the novel Li<sub>2</sub>S-Li<sub>3</sub>P solid solutions. These novel ternary compounds exhibit significantly higher ionic conductivities compared to Li<sub>2</sub>S, primarily due to the incorporation of phosphorus atoms. In these ternary compounds, each phosphorus atom substitutes a sulphur atom, occupying a 4a site. Phosphorus atoms, with their 3<sup>-</sup> oxidation state, exert stronger Coulombic interactions with lithium ions compared to sulphur atoms with a 2<sup>-</sup> oxidation state. This interaction not only stabilises the adjacent 4b sites, enabling the coordination of additional lithium atoms, as depicted in the upper panel of **Figure 2c**, but also reduces the energy barrier for T-O migration. Consequently, diffusion channels primarily form around the phosphorus atoms due to the increased availability of stable interstitial sites. Notably, most lithium diffusion in these ternary compounds occurs

in the vicinity of phosphorus atoms, as demonstrated in the bulk-Li<sub>7</sub>PS<sub>2</sub> structure shown in the lower panel of **Figure 2c**. Substituting S sites with P does not appear to alter the 3D Li migration pathways significantly, as both T-T (more visible in other ternaries) and T-O-T paths (but not O-O) are utilised in all ternaries. A clear distinction between the parent Li<sub>2</sub>S and the Li<sub>2</sub>S-Li<sub>3</sub>P solutions is the significantly higher prevalence of T-O-T (8c-4b-8c) conduction channels even at low temperatures, making the T-O-T path the primary mode of conduction. This is likely facilitated by the additional interstitial Li ions. The limited number of 4b sites makes the phosphorus-to-sulphur ratio a critical factor in optimising ionic conduction. **Figure 2d** shows the calculated lithium ion conductivity at 525 K as a function of phosphorus content. Li<sub>2</sub>S and Li<sub>3</sub>P, representing the extremes, exhibit negligible conductivity. The data indicate that conductivity peaks around a phosphorus content of 50 % (Li<sub>5</sub>PS) where the phosphorus atoms are anticipated to distribute throughout the electrolyte more homogenously. Insufficient phosphorus results in a low number of stabilised 4b sites, reducing the number of available hopping sites for lithium ions. Conversely, an excess of phosphorus leads to an over-coordination of lithium ions, decreasing the number of vacant, stable 4b sites and thus limiting ionic conduction.

Based on these findings, we propose that incorporating phosphorus sites into the Li<sub>2</sub>S-Li<sub>3</sub>P solutions enhances Li migration through two mechanisms: (1) by lowering the migration energy barrier between nearby 8c-4b (T-O) sites due to strong Coulomb interactions between Li<sup>+</sup>-P<sup>3-</sup> ions, and (2) by coordinating additional Li ions at the higher-energy interstitial octahedral (4b) sites. The former mechanism aligns with previous reports on other superionic conductors.<sup>61</sup> Both factors facilitate migration along the 8c-4b-8c and 8c-8c paths, with the former being more prominent, while the 4b-4b path remains less populated.

### 3.2. Surface formation

Surface formation energy is a crucial parameter in materials science, quantifying the stability of a surface relative to the bulk material. *Ab-initio* simulations, rooted in quantum mechanics, offer a powerful means to compute this energy. For this, the bulk and surface (slab) structures are modelled at the atomic level and their total energies are calculated separately. By comparing these energies, the surface formation energy ( $\gamma_s$ ) can be derived as the energy difference between the surface and the corresponding bulk per unit area as follows

$$\gamma_s = \frac{(E_{\text{slab}} - n \cdot E_{\text{bulk}})}{2A} \quad (4).$$

Here,  $E_{\text{slab}}$  is the total energy of the slab,  $E_{\text{bulk}}$  is the energy of the bulk crystal per formula unit,  $n$  is the number of formula units in the slab model and  $2A$  is the surface area of the two surfaces of the slab. The accuracy of this formula depends on the presence of symmetrical surfaces within the slab and the preservation of stoichiometric ratio of the elements. However, in instances where keeping the symmetry necessitates the breach of stoichiometry or where imposing symmetry proves unattainable, alternative considerations arise. In scenarios where breaking stoichiometry is necessary, the calculation of surface formation energy can be achieved by adapting the formula to incorporate chemical potentials associated with specific species (chemical potentials pertaining to individual elements or a predetermined set of molecules). This modification is essential to accommodate the energy contributions introduced by additional / missing atoms, and it can be expressed as follows:

$$\gamma_s = \frac{\left( E_{\text{slab}} - \left( n \cdot E_{\text{bulk}} + \sum_{i=1}^j c_i \mu_i \right) \right)}{2A} \quad (5),$$

where  $j$  is the number of different kinds of the extra elements,  $c_i$  and  $\mu_i$  are the number and chemical potential of the extra element of kind  $i$ , respectively. The inherent issue with this methodology lies in the non-uniqueness of the chemical potential values assigned to specific elements. Conventionally, the determination of chemical potentials involves evaluating the energies associated with a range of constituent subsystems that collectively form the overarching structure. The selection of these subsystems can vary, and there is no consensus on the optimal approach. For instance, Xie et al.<sup>62</sup> adopt a phase diagram-based approach, selecting subsystems from the end members of the tie line in which the final product lies, while Canepa et al.<sup>63</sup> and Gao et al.<sup>64</sup> utilize the decomposition products as subsystems for chemical potential calculations (decomposition approach). Another strategy involves using the bulk forms of the elements (elemental approach), although for some cases this may yield high inaccuracy due to the presence of numerous intermediate structures between bulk elements and the final product as well as of ill-defined chemical potentials for gaseous species. Alternatively, starting materials for the final structure can serve as the basis for subsystem selection (starting material approach). Karasulu et al.<sup>65</sup> demonstrated in their investigation of the LLZO system that the last two approaches indeed produce different values for chemical potentials and formation energies, albeit without altering the ordering of formation energies. The lack of empirical methods to check the validity of these diverse set of chemical potentials leads to a significant ambiguity.

In our study, we assess the chemical potentials associated with lithium (Li), sulphur (S), and phosphorus (P) atoms using the decomposition approach, analysing energies inherent to bulk lithium, lithium sulphide ( $\text{Li}_2\text{S}$ ), and lithium phosphide ( $\text{Li}_3\text{P}$ ), or alternatively, employing the starting material approach, analysing lithium sulphide, lithium phosphide, and phosphorus pentasulfide ( $\text{P}_2\text{S}_5$ ), as well as the elemental approach, analysing bulk lithium (bcc-Li), bulk sulphur, and bulk phosphorus (black phosphorus). Each distinct configuration of these subsystems yields disparate chemical potentials, necessitating comparison with experimental data to validate their accuracy. However, due to significant disparities observed in the formation energies of the structures studied in this work when employing chemical potentials derived from the aforementioned set of subsystems (see Supplementary Information, **Table S1** and **Table S2**), we have opted to forgo the incorporation of chemical potential considerations and instead maintain consistent stoichiometry across all scenarios (even if it results in symmetry-breaking in some cases).

As previously stated, the determination of surface formation energy necessitates the utilization of symmetric surfaces, a requirement that may not be generally achievable across all Miller indices. Indeed, the presence of symmetric surfaces within the systems under investigation is notably scarce. Consequently, we have devised a methodological approach guided by a predefined set of principles governing the generation of slabs, with particular emphasis on prioritizing specific surface characteristics.

The set of principles can be outlined as follows:

1. Ensuring stoichiometric integrity of the slabs: This principle arises from the inherent non-uniqueness of chemical potential selections (and the lack of testing mechanisms), where outcomes are intricately tied to the chosen parameters, as previously discussed.
2. Where feasible, striving for the creation of symmetric surfaces: Surface symmetry is imperative for the application of **Eqn 4**, facilitating the precise determination of surface formation energies. The slabs featuring symmetric surfaces are denoted by the symbol "s" within **Table 1**.
3. In instances where symmetric surfaces are unattainable, a strategy is adopted to align surface atoms while disregarding those situated beneath. This approach aims to maximize symmetry

within the outermost layers (while minimizing the net dipole moment), thereby enabling the utilization of **Eqn 4** under the assumption of comparable formation energies between the two surfaces. The slabs featuring quasi-symmetric surfaces are denoted by the symbol "q" within **Table 1**.

4. While not a strict rule, it is practical to maintain the integrity of the S-P bonds in  $\text{PS}_4$  tetrahedra (if any) during surface formation to prevent substantial energy penalties.
5. In cases where neither symmetric nor quasi-symmetric surfaces can be achieved, the surfaces are constructed while adhering solely to stoichiometric considerations, with subsequent evaluation to ascertain if the resulting average energy is lower than alternative configurations. For the structures in this category, the results will only be meaningful if the calculated formation energy for the fully non-symmetric slab is found to be the lowest among all Miller indices indicating the need for subsequent investigation into the corresponding structure. Fully non-symmetric slabs are denoted by the symbol "n" within **Table 1**.

**Table 1:** Calculated surface formation energies of the studied material systems using various Miller indices. Symmetry of the slab surfaces: s = symmetric, q = quasi-symmetric, n = fully non-symmetric

$\gamma_s$ (J/m <sup>2</sup> )	Li	$\text{Li}_3\text{P}$	$\gamma\text{-Li}_3\text{PS}_4$	$\text{Li}_7\text{P}_3\text{S}_{11}$	$\text{Li}_2\text{S}$	$\text{Li}_7\text{PS}_2$	$\text{Li}_5\text{PS}$	$\text{Li}_8\text{P}_2\text{S}$	$\text{Li}_{11}\text{P}_3\text{S}$
(001)	<b>0.46<sup>s</sup></b>	<b>0.48<sup>s</sup></b>	0.45 <sup>q</sup>	0.25 <sup>s</sup>	0.88 <sup>s</sup>	0.65 <sup>q</sup>	0.65 <sup>s</sup>	0.65 <sup>q</sup>	0.71 <sup>q</sup>
(010)			0.21 <sup>s</sup>	0.18 <sup>s</sup>		0.67 <sup>q</sup>	0.67 <sup>s</sup>	0.66 <sup>q</sup>	0.68 <sup>q</sup>
(100)		0.51 <sup>s</sup>	0.34 <sup>s</sup>	<b>0.09<sup>s</sup></b>		0.66 <sup>q</sup>	0.61 <sup>s</sup>	0.65 <sup>q</sup>	0.74 <sup>q</sup>
(011)	0.50 <sup>s</sup>	0.67 <sup>s</sup>	0.41 <sup>q</sup>	0.12 <sup>s</sup>	0.50 <sup>s</sup>	0.51 <sup>q</sup>	0.56 <sup>s</sup>	0.59 <sup>q</sup>	0.65 <sup>q</sup>
(01 $\bar{1}$ )			0.40 <sup>n</sup>	0.17 <sup>s</sup>		0.50 <sup>q</sup>	0.56 <sup>s</sup>	0.62 <sup>q</sup>	0.64 <sup>q</sup>
(101)			0.27 <sup>q</sup>	0.12 <sup>s</sup>		0.51 <sup>q</sup>	0.59 <sup>s</sup>	0.57 <sup>q</sup>	0.69 <sup>q</sup>
(10 $\bar{1}$ )			0.46 <sup>n</sup>	0.15 <sup>s</sup>		0.55 <sup>q</sup>	0.59 <sup>s</sup>	0.58 <sup>q</sup>	0.59 <sup>q</sup>
(110)		0.73 <sup>s</sup>	<b>0.18<sup>s</sup></b>	0.20 <sup>s</sup>		0.53 <sup>q</sup>	0.62 <sup>s</sup>	0.60 <sup>q</sup>	0.66 <sup>q</sup>
(1 $\bar{1}$ 0)			0.18 <sup>s</sup>	0.20 <sup>s</sup>		0.55 <sup>q</sup>	0.62 <sup>s</sup>	0.57 <sup>q</sup>	0.65 <sup>q</sup>
(111)	0.54 <sup>s</sup>	0.85 <sup>s</sup>	0.33 <sup>n</sup>	0.18 <sup>s</sup>	<b>0.33<sup>s</sup></b>	<b>0.34<sup>q</sup></b>	<b>0.43<sup>s</sup></b>	0.46 <sup>q</sup>	0.56 <sup>q</sup>
(11 $\bar{1}$ )			0.29 <sup>n</sup>	0.16 <sup>s</sup>		0.36 <sup>q</sup>	0.43 <sup>s</sup>	<b>0.42<sup>q</sup></b>	<b>0.54<sup>q</sup></b>
(1 $\bar{1}$ 1)			0.36 <sup>n</sup>	0.17 <sup>s</sup>		0.34 <sup>q</sup>	0.43 <sup>s</sup>	0.43 <sup>q</sup>	0.58 <sup>q</sup>
( $\bar{1}$ 11)			0.50 <sup>n</sup>	0.13 <sup>s</sup>		0.37 <sup>q</sup>	0.43 <sup>s</sup>	0.44 <sup>q</sup>	0.56 <sup>q</sup>
(11 $\bar{2}$ )				0.22 <sup>s</sup>					
(10 $\bar{2}$ )				0.21 <sup>s</sup>					
(210)	0.51 <sup>s</sup>		0.54 <sup>s</sup>						
(211)	0.54 <sup>s</sup>		0.29 <sup>n</sup>						

We systematically studied the free surface formation for bcc-Li, Li<sub>3</sub>P,  $\gamma$ -Li<sub>3</sub>PS<sub>4</sub>, Li<sub>7</sub>P<sub>3</sub>S<sub>11</sub>, Li<sub>2</sub>S and the new ternaries (Li<sub>7</sub>PS<sub>2</sub>, Li<sub>5</sub>PS, Li<sub>8</sub>P<sub>2</sub>S, Li<sub>11</sub>P<sub>3</sub>S) for all Miller indices up to 1 (i.e., -1,0,1). For some cases, we further analyzed specific Miller indices to compare with the literature. The results are presented in **Table 1** where we show the lowest formation energies in bold font. (001) surface in metallic bcc-Li (equivalent to (100) surface due to symmetry) and (001) surface in Li<sub>3</sub>P present the lowest formation energies of 0.46 J/m<sup>2</sup> and 0.48 J/m<sup>2</sup>, respectively, which are in perfect agreement with previous studies.<sup>66-68</sup> The surfaces of  $\gamma$ -Li<sub>3</sub>PS<sub>4</sub> have not been extensively explored in the literature. Lepley et al.<sup>69</sup> reported a surface formation energy of 0.32 J/m<sup>2</sup> for the (010) surface. However, our calculations yield a lower formation energy of 0.21 J/m<sup>2</sup> for the same (010) surface. Discrepancies in energy assessments may stem from the myriad of conceivable surfaces for Li<sub>3</sub>PS<sub>4</sub>, rendering comprehensive analysis impractical. For instance, the (010) surface presents at least three distinct cuts, the fewest among all Miller indices, further compounded by the lack of symmetry in many slabs, introducing additional ambiguity to model selection and ensuing energy calculations. Our results indicate that the (110) surface has the lowest surface energy, at 0.18 J/m<sup>2</sup>, suggesting it is the most stable surface orientation in  $\gamma$ -Li<sub>3</sub>PS<sub>4</sub>. For Li<sub>7</sub>P<sub>3</sub>S<sub>11</sub>, (100) surface yields the lowest surface formation energy of 0.09 J/m<sup>2</sup>, consistent with prior literature.<sup>70</sup> Due to the cubic symmetry of Li<sub>2</sub>S, our study focuses on the formation of surfaces corresponding to three Miller indices: (100), (110), and (111). Although the cubic symmetry is disrupted in the new ternary compounds, their structural framework remains analogous to Li<sub>2</sub>S. Consequently, their surfaces can be categorized into three distinct families of Miller indices, as illustrated in **Figure 3**. Specifically, the (100) family includes (010) and (001) surfaces; the (110) family includes (1 $\bar{1}$ 0), (101), (10 $\bar{1}$ ), (011), and (01 $\bar{1}$ ) surfaces; and the (111) family includes (11 $\bar{1}$ ), (1 $\bar{1}$ 1), and (111) surfaces. The families are identified by their structural motifs at the surface. However, one can also identify these families by the motifs of the side view (**Figure 3**). For example, in (100) family, both closest anions and cations form a square shape from side view, whereas, in (110) family, anions form a parallelogram and cations form a rectangle. Although the surfaces within each family are not equivalent, they exhibit similar surface formation energies within the family (**Table 1**). The (111) surface of Li<sub>2</sub>S demonstrates the lowest formation energy at 0.33 J/m<sup>2</sup>, which aligns well with values reported in the literature.<sup>62,66,68</sup> The red circles and lines on the far left of **Figure 3** represent the Li atoms and Li-S bonds lost during the cleavage to create the surface. Notably, for the (111) surface, sulphur atoms lose only a single Li bond, whereas for the (100) and (110) surfaces, two Li bonds are broken. We note that the breaking of fewer bonds during surface formation leads to a smaller increase in total energy, which in turn results in lower formation energy. Given the similar framework to Li<sub>2</sub>S, the new ternary compounds also exhibit the lowest surface formation energies for (111) type surfaces. Specifically, for Li<sub>7</sub>PS<sub>2</sub> and Li<sub>5</sub>PS, the (111) surfaces have the lowest formation energies of 0.34 J/m<sup>2</sup> and 0.43 J/m<sup>2</sup>, respectively while, the lowest formation energy for Li<sub>8</sub>P<sub>2</sub>S and Li<sub>11</sub>P<sub>3</sub>S is observed for the (11 $\bar{1}$ ) surfaces, with values of 0.42 J/m<sup>2</sup> and 0.54 J/m<sup>2</sup>, respectively. Notably, the surface formation energy increases with the phosphorus content. In these systems, each phosphorus ion can coordinate additional lithium ions. Consequently, when the bulk structure is cleaved to form a surface, the phosphorus ions at the surface lose more lithium coordination than sulphur ions. This implies that with higher phosphorus content, more P-Li bonds are broken upon surface formation, thereby increasing the surface formation energy.

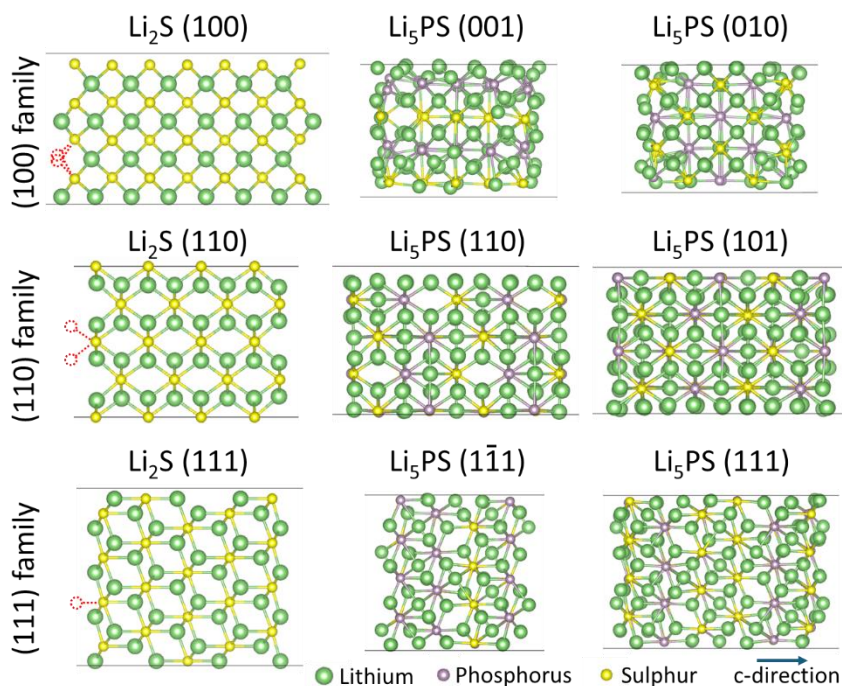


**Figure 3.** Three distinct families of surfaces as identified by their unique Miller indices for  $\text{Li}_2\text{S}$  and the new ternaries. The families can be distinguished by the structural motives they encompass. The red lines and circles represent Li-S bond and Li atoms lost due to cutting to form the surface.

The Wulff construction, or Wulff shape, is a geometric method utilized to ascertain the equilibrium morphology of a crystal.<sup>71,72</sup> This method is predicated on the principle that the growth or shrinkage of each crystal facet is proportional to its surface formation energy. The construction process involves plotting the surface energy as a function of the orientation of the crystal faces and creating a polar plot from the origin with radii proportional to these surface energies. The inner envelope of these radii, known as the Wulff shape, represents the crystal's equilibrium morphology. This shape provides critical insights into the stability and growth patterns of crystals, as facets with lower surface energy are more prominent in the equilibrium shape. The Wulff construction is a fundamental concept in materials science, crystallography, and surface science, offering a theoretical framework for predicting the macroscopic shape of crystalline materials based on microscopic surface properties.

In **Figure 4**, we present the Wulff shapes derived from the surface formation energies listed in Table 1. The shape for bcc-Li aligns perfectly with the literature,<sup>67</sup> showing (001) and (110) surfaces contributing 39% and 34% of the total surface area, respectively. Contributions from (111), (210), and (211) are approximately 9% each. The shape for  $\text{Li}_3\text{P}$  shows some differences from what Canepa et. al.<sup>66</sup> obtained because they also investigate Miller indices higher than 1. The Wulff shape for  $\text{Li}_3\text{P}$  is composed of (100) and (001) type surfaces, with 65% and 35% surface areas, respectively. (110) and (101) surfaces dominate the Wulff shape of  $\gamma\text{-Li}_3\text{PS}_4$  by contributing 58% and 33% to the surface area, respectively. For  $\text{Li}_7\text{P}_3\text{S}_{11}$ , the surface area contributions are more evenly distributed, with (100) surface contributing 31%, (011) surface 19%, (101) surface 16%, and (111) surface 13%. For  $\text{Li}_2\text{S}$ , the Wulff shape exclusively contains the (111) surface. In new ternaries, similar to  $\text{Li}_2\text{S}$ , the Wulff shape is dominated by the (111) family surfaces. However, as the phosphorus content increases, other surface families begin to appear, resulting in a less anisotropic shape. This is attributed to the rapid increase in surface formation energy for the (111) family

with increasing phosphorus content. For  $\text{Li}_{11}\text{P}_3\text{S}$ , the Wulff shape comprises (111), (100), and (110) surfaces, contributing 78%, 14%, and 8% to the total area, respectively.

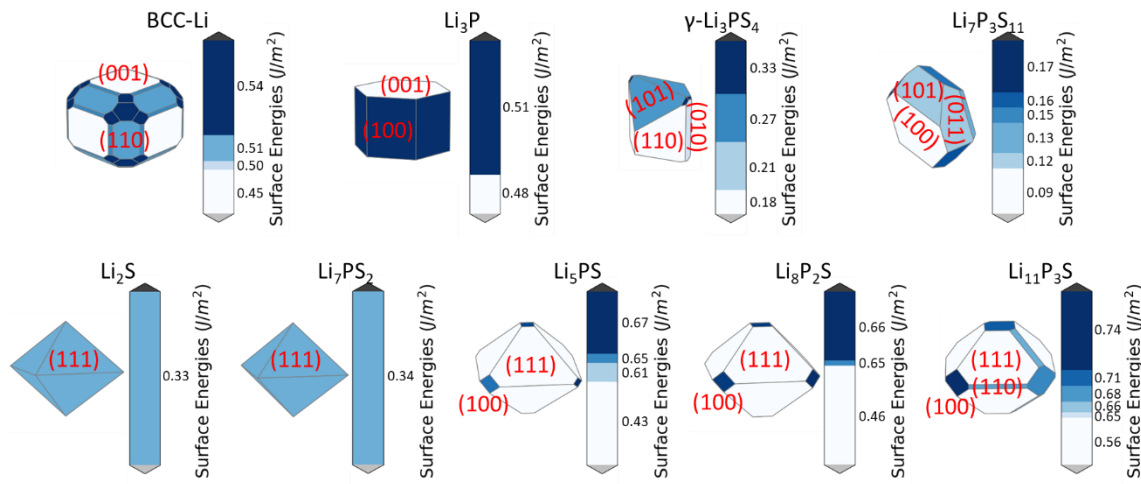


**Figure 4.** Wulff Shapes for all of the studied material systems.

### 3.3. Interface stability at 0K

Upon elucidating the surface formation energies for Li-P-S surfaces, we employed the INTERFACER<sup>48</sup> computational framework to construct interfaces between Li(100) and various Li-P-S surfaces ensuring minimal surface formation energies (see the values in bold font in **Table 1**).

The total interface formation energy for any interface between materials *a* and *b* can be calculated as follows;

$$\gamma_{ab} = \frac{E_{ab} - (n_a E_a + n_b E_b)}{2A} \quad (6),$$

where  $E_{ab}$  signifies the total energy of the interface system,  $n_a$  ( $n_b$ ) denotes the number of formula units of material *a* (*b*), with corresponding total energy of  $E_a$  ( $E_b$ ) per formula unit, and  $A$  represents the surface area of the interface. The division by  $2A$  accounts for the presence of two interfaces in the sandwich model (with no vacuum padding between surface slabs).

Due to the imposed boundary conditions in the simulation system, a lattice strain is artificially introduced while aligning the lattices of materials *a* and *b*. However, in real materials, such boundary conditions are absent, potentially resulting in minimal or negligible strain. Consequently, the calculated interface formation energy is usually overestimated, encapsulating an energy component attributed to in-plane strain. The actual interface energy ( $\gamma_{ab}^{act}$ ) therefore exists within upper and lower bounds represented as  $\gamma_{ab}^{min} < \gamma_{ab}^{act} < \gamma_{ab}^{max}$ , where  $\gamma_{ab}^{max} = \gamma_{ab}^{\square}$  and  $\gamma_{ab}^{min}$  denotes the minimal interface energy devoid of strain energy ( $E^{str}$ ), calculated as;

$$\gamma_{ab}^{min} = \gamma_{ab} - E^{str} \quad (7).$$

The strain energy can be determined through various methods but we introduce only two of them here. The first method involves subtracting the energy of relaxed slabs from that of strained slabs. Similar to the methodology employed by Ferrari et al.,<sup>73</sup> where the lattice parameters of the interface were fixed to the bulk lattice parameters of one system, here, we allow interface structure to relax to its minimum energy configuration, inducing strain in both slabs. Thus, the strain energy for each slab can be calculated as follows

$$E_{\text{slab}-a}^{\text{str}} = \frac{E_{\text{slab}-a}^{\text{strained}} - E_{\text{slab}-a}^{\text{relaxed}}}{2A} \quad (8),$$

where  $E_{\text{slab}-a}^{\text{strained}}$  is the energy of “slab  $a$ ” which is under strain and  $E_{\text{slab}-a}^{\text{relaxed}}$  is the energy of the same slab when the in-plane lattice vectors are allowed to relax. Since this method uses slabs, it ignores any contribution that may arise due to the presence of the system  $b$ , i.e. the interface. The second, more rigorous method, proposed by Lepley et al.,<sup>74</sup> incorporates the contribution of the interface on strain. It calculates the in-plane strain caused by lattice mismatch at the interface between materials  $a$  and  $b$  as:

$$\gamma_{ab} = \gamma_{ab}^{\text{lim}} + n_b c \quad (9),$$

where  $\gamma_{ab}^{\text{lim}}$  is the interface energy in the coherent limit,  $n_b$  is the number of formula units of material  $b$  and  $c$  is a constant that is dependent of the material and the applied stress. This formula assumes that the lattices of the interface systems are fixed to the bulk values of material  $a$  and only material  $b$  is under strain. For the formula above, plotting  $\gamma_{ab}$  against  $n_b$  should yield a straight line with slope  $c$  and intercept  $\gamma_{ab}^{\text{lim}}$ . However, since our interface simulations involve relaxation of the entire system rather than fixing the lattices to bulk values of one material, **Eqn 9** is modified to include strain in both materials as:

$$\gamma_{ab} = \gamma_{ab}^{\text{lim}} + n_a c_a + n_b c_b \quad (10).$$

Here, plotting  $\gamma_{ab}$  against  $n_a$  ( $n_b$ ) should yield a straight line with slope  $c_a$  ( $c_b$ ) and intercept  $\gamma_{ab}^{\text{lim}} + n_b c_b$  ( $\gamma_{ab}^{\text{lim}} + n_a c_a$ ) as shown in **Figure 5**. Consequently, the strain values for each material  $E_a^{\text{str}} = n_a c_a$  ( $E_b^{\text{str}} = n_b c_b$ ) can be calculated, and the total strain ( $E^{\text{str}}$ ) can be determined as the sum of individual strains.  $\gamma_{ab}^{\text{lim}}$  can then be calculated by inserting individual strain values into **Eqn 10**. The difference between  $\gamma_{ab}^{\text{min}}$  and  $\gamma_{ab}^{\text{lim}}$  obtained from the two approaches describes the contribution of the interface to strain energy.

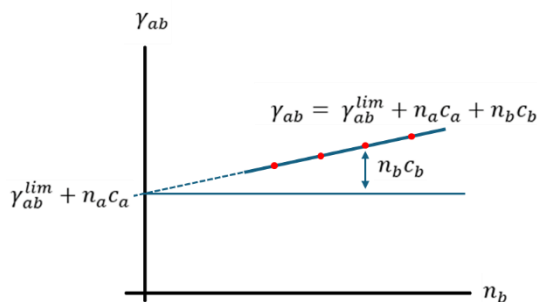


**Figure 5.** A schematic plot to illustrate the calculation of strain using **Eqn 10** via the linear change of interface formation energy as a function of the thickness of slab  $b$ .

A significant limitation of the second method is the rapid escalation in the number of atoms as  $n$  is increased for the Li-P-S systems. For the majority of the interfaces we examine, we employ the minimal  $n$  values for Li-P-S slabs, which are already considerably thick. Consequently, this renders the second approach impractical for our purposes. Nevertheless, we conducted a series of tests using second method to evaluate the differential impacts between the two methodologies. To this end, we calculated the strain energy using both methodologies (**Eqn 8** and **Eqn 10**) for two exemplary systems: Li<sub>2</sub>S(111) // Li(100) and Li<sub>5</sub>PS(111) // Li(100). The results are summarized in **Table 2**. The strain values obtained from both methodologies are of the same order, and the difference between the minimum interface formation energies without strain is less than 10%. Therefore, we applied the first methodology to the remainder of the interfaces studied.

**Table 2.** Calculated strain energies with two methodologies, i.e. using **Eqn 8** and **Eqn 10**.

(J/m <sup>2</sup> )							
Li <sub>2</sub> S(111) // Li(100)	$E_{Li}^{str}$	$E_{Li_2S}^{str}$	$E_{\square}^{str}$	$\gamma_{\square}^{min} (\gamma_{\square}^{lim})$	Difference (%)	$c_{Li}^{\square}$	$c_{Li_2S}^{\square}$
From Eqn 8	$2.9 \times 10^{-2}$	$5.4 \times 10^{-2}$	$8.3 \times 10^{-2}$	0.31	1.5		
From Eqn 10	$3.2 \times 10^{-2}$	$4.6 \times 10^{-2}$	$7.9 \times 10^{-2}$	0.32		$1.3 \times 10^{-4}$	$6.8 \times 10^{-4}$
Li <sub>5</sub> PS(111) // Li(100)	$E_{Li}^{str}$	$E_{Li_5PS}^{str}$	$E_{\square}^{str}$	$\gamma_{\square}^{min} (\gamma_{\square}^{lim})$	Difference (%)	$c_{Li}^{\square}$	$c_{Li_5PS}^{\square}$
From Eqn 8	$6.1 \times 10^{-2}$	$8.8 \times 10^{-2}$	0.15	0.14	7.5		
From Eqn 10	$5.6 \times 10^{-2}$	$8.0 \times 10^{-2}$	0.14	0.15		$3.8 \times 10^{-4}$	$1.7 \times 10^{-3}$

The work of adhesion represents the energy required to separate two adherent surfaces to an infinite distance and quantifies the mechanical stability of an interface. In practical terms, for our purposes, the work of adhesion is defined as the energy necessary to separate the two slabs and can be formulated as follows,

$$W_{adh}^{min} = \frac{(E_{slab-a} + E_{slab-b}) - E_{ab}}{2A} \quad (11).$$

We define  $W_{adh}^{min}$  as the minimum work of adhesion because similar to interface formation energy, it inherently contains the strain energy which lowers the value. To get the maximum work of adhesion, we need to add the strain energy to this minimum value ( $W_{adh}^{max} = W_{adh}^{min} + E_{\square}^{str}$ ). Similar to the interface formation energy, the actual work of adhesion lies between  $W_{adh}^{min}$  and  $W_{adh}^{max}$ . Typically, low (positive) interfacial energy and high (positive) work of adhesion are indicative of strong interfacial stability.

The calculated values for the interface formation energy, work of adhesion and strain energy are summarized in **Table 3**. The calculated maximum and minimum formation energies for Li<sub>3</sub>P(001) // Li(100) and Li<sub>2</sub>S(111) // Li(100) interfaces are  $\gamma_{Li_3P//Li}^{max} = 0.37 \text{ J/m}^2$ ,  $\gamma_{Li_3P//Li}^{min} = 0.35 \text{ J/m}^2$ ,  $\gamma_{Li_2S//Li}^{max} = 0.40 \text{ J/m}^2$  and  $\gamma_{Li_2S//Li}^{min} = 0.31 \text{ J/m}^2$ , respectively, which are in agreement with the literature.<sup>66</sup> The interface formation energies for new ternaries are even lower than Li<sub>2</sub>S and Li<sub>3</sub>P, indicating higher stability. Interface formation energies are typically positive because the formation of interfaces involves creating

surfaces from the bulk forms of two systems, which are inherently lower in energy. However, the interfaces of  $\text{Li}_3\text{PS}_4$  and  $\text{Li}_7\text{P}_3\text{S}_{11}$  with Li metal exhibit negative interface formation energies. This anomaly indicates that the interface is active, with some chemical interactions occurring that lower the total energy of the interface system. We present the  $\text{Li}_5\text{PS} // \text{Li}$  and  $\text{Li}_7\text{P}_3\text{S}_{11} // \text{Li}$  interfaces as examples of inactive and active interfaces, respectively, in **Figure 6**. The dashed lines indicate the position of the interface before relaxation. Notably, the  $\text{PS}_4$  tetrahedra near the interface breaks up and sulphur atoms diffuse across the  $\text{Li}_7\text{P}_3\text{S}_{11} // \text{Li}$  interface to coordinate with lithium atoms and form  $\text{Li}_2\text{S}$ -like structures as indicated by the oval (**Figure 6, bottom panel**), whereas no diffusion of sulphur or phosphorus atoms is observed across the  $\text{Li}_5\text{PS} // \text{Li}$  interface (**top panel**). The sulphur atom diffusion results in the breaking of S-P bonds. Then, undercoordinated phosphorus atoms bond with lithium atoms in the vicinity. These changes in the bond formation from P-S to P-Li and S-Li significantly reduce the total energy of the system, leading to negative formation energy. The works in the literature that study the apparent reactivity of  $\text{Li}_3\text{PS}_4 // \text{Li}$  and  $\text{Li}_7\text{P}_3\text{S}_{11} // \text{Li}$  interfaces agree on the formation of a similar  $\text{Li}_2\text{S}$ -like buffer layer.<sup>69,73-76</sup>

The calculated maximum and minimum work of adhesion for  $\text{Li}_3\text{P}(001) // \text{Li}(100)$  and  $\text{Li}_2\text{S}(111) // \text{Li}(100)$  interfaces are  $W_{\text{Li}_3\text{P}/\text{Li}}^{\max} = 0.58 \text{ J/m}^2$ ,  $W_{\text{Li}_3\text{P}/\text{Li}}^{\min} = 0.56 \text{ J/m}^2$ ,  $W_{\text{Li}_2\text{S}/\text{Li}}^{\max} = 0.50 \text{ eV/nm}^2$  and  $W_{\text{Li}_2\text{S}/\text{Li}}^{\min} = 0.42 \text{ eV/nm}^2$ , respectively, which are consistent with the values reported in the literature.<sup>66,68</sup> The work of adhesion for the new ternary compounds with lithium is higher than that for  $\text{Li}_2\text{S}$  and  $\text{Li}_3\text{P}$ , indicating greater stability. Furthermore, the work of adhesion for the new ternary compounds with lithium increases with the phosphorus content, similar to the trend observed for surface formation energy. Phosphorus atoms can coordinate more lithium atoms than sulphur atoms can, resulting in the formation of more bonds at the interface, making it more difficult to separate the surfaces. In the cases of  $\text{Li}_3\text{PS}_4 // \text{Li}$  and  $\text{Li}_7\text{P}_3\text{S}_{11} // \text{Li}$  interfaces, the chemical reactions at the interface lead to a significant reduction in energy, yielding much higher work of adhesion compared to the other interfaces discussed.

**Table 3.** Calculated maximum and minimum interface formation energies ( $\gamma_{ab}^{\max}, \gamma_{ab}^{\min}$ ), adhesive energies ( $W_{adh}^{\max}, W_{adh}^{\min}$ ) and the strain energy (from the first method) for Li-P-S systems against  $\text{Li}(100)$ , all energies in  $\text{J/m}^2$ .

( $\text{J/m}^2$ )	$\gamma_{ab}^{\max}$	$\gamma_{ab}^{\min}$	$W_{adh}^{\min}$	$W_{adh}^{\max}$	$E_{\square}^{str}$
$\text{Li}_3\text{P}(001) // \text{Li}(100)$	0.37	0.35	0.56	0.58	$2.0 \times 10^{-2}$
$\gamma\text{-Li}_3\text{PS}_4(110) // \text{Li}(100)$	-0.90	-1.11	1.41	1.63	0.22
$\text{Li}_7\text{P}_3\text{S}_{11}(100) // \text{Li}(100)$	-1.87	-2.04	2.31	2.48	0.17
$\text{Li}_2\text{S}(111) // \text{Li}(100)$	0.40	0.31	0.42	0.50	$8.3 \times 10^{-2}$
$\text{Li}_7\text{PS}_2(111) // \text{Li}(100)$	0.27	0.25	0.50	0.52	$1.9 \times 10^{-2}$
$\text{Li}_5\text{PS}(111) // \text{Li}(100)$	0.28	0.14	0.49	0.64	0.15
$\text{Li}_8\text{P}_2\text{S}(111) // \text{Li}(100)$	0.25	0.22	0.56	0.60	$3.2 \times 10^{-2}$
$\text{Li}_{11}\text{P}_3\text{S}(111) // \text{Li}(100)$	0.28	0.15	0.58	0.74	0.13

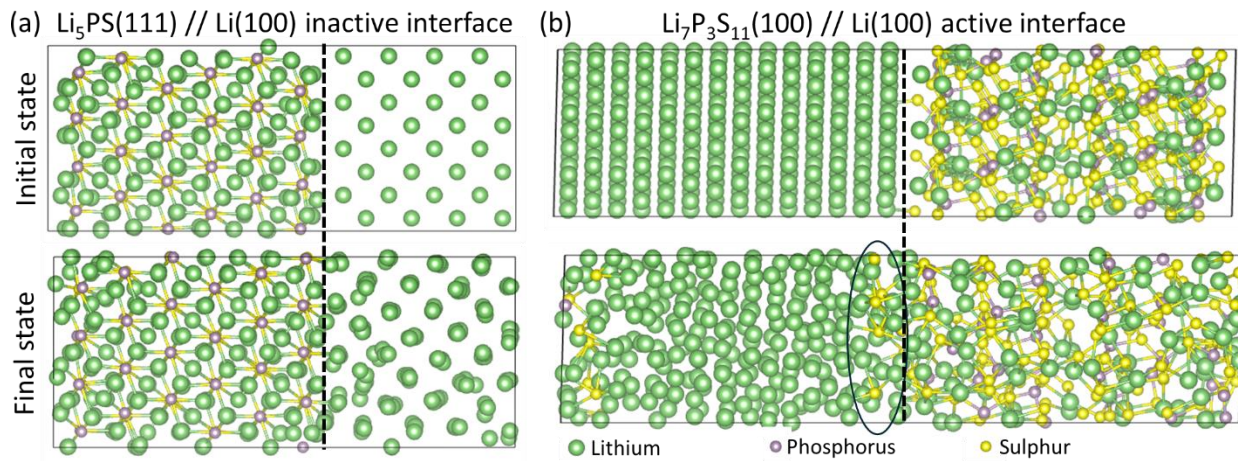


**Figure 6.** The initial and the final (relaxed) states of a) chemically inactive  $\text{Li}_5\text{PS}$  // Li, and b) chemically active  $\text{Li}_7\text{P}_3\text{S}_{11}$  // Li interface structures. The dashed black line indicates the initial position of the interface. The black oval highlights the sulphur diffusion into lithium metal.

### 3.4. Dynamic interface stability at finite temperature

In our study, we employed AIMD simulations to investigate the chemical interactions and stability of interfaces between Li-metal anode and the electrolytes as well as the effects of the interface on diffusion properties of Li ions at finite temperatures, with a particular emphasis on the formation of SEI layers. This state-of-the-art computational technique enables precise modelling of atomic interactions by solving the fundamental equations of quantum mechanics, thereby providing superior accuracy compared to classical molecular dynamics (MD) and continuum models. Unlike classical MD, which relies on empirical force fields, AIMD does not necessitate predefined potential functions, allowing for a detailed description of complex chemical processes and electronic structure variations at atomic scale. Despite the computational expense limiting AIMD simulations to timescales of hundreds of picoseconds and system sizes to approximately 1000 atoms or fewer, these simulations furnish sufficient data to facilitate comparative analyses of different interfaces. By simulating the behaviour of these solid-solid interfaces under diverse thermal conditions, we obtain critical insights into their structural integrity, dynamical properties, and the mechanisms governing SEI layer formation. This information is crucial for the design and optimization of materials in advanced energy storage systems, where the stability of electrode-electrolyte interfaces and the dynamics of SEI layers are vital for ensuring optimal performance and longevity. In this section, we focus on the chemical interactions and the dynamical stability of the interfaces.

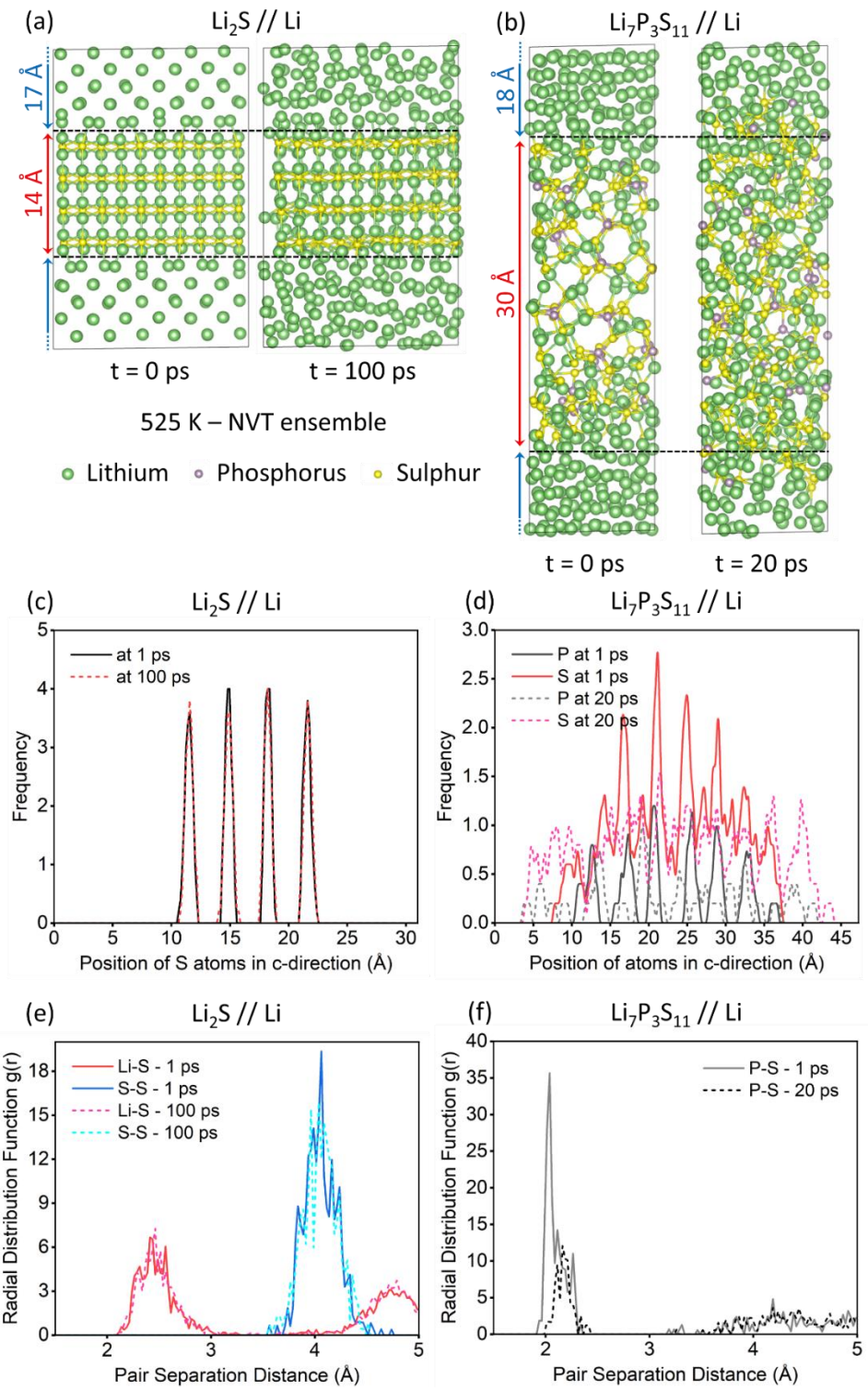


**Figure 7.** Evolution of the microstructure for a)  $\text{Li}_2\text{S} // \text{Li}$  and b)  $\text{Li}_7\text{P}_3\text{S}_{11} // \text{Li}$  interface structures at 525 K. Black dashed lines indicate the positions of the initial interface in a) and b). The positional histogram of P and S atoms along c-axis (perpendicular to the interface) for c)  $\text{Li}_2\text{S} // \text{Li}$  and d)  $\text{Li}_7\text{P}_3\text{S}_{11} // \text{Li}$  interface structures. The pair distributions of certain atomic pairs for e)  $\text{Li}_2\text{S} // \text{Li}$  and f)  $\text{Li}_7\text{P}_3\text{S}_{11} // \text{Li}$  interface structures.

### 3.4.1. Stability of established Li-P-S electrolytes

First, we systematically investigated the time evolution of the intricate interfaces formed between lithium anode and commonly-studied lithium thiophosphate electrolytes, namely  $\text{Li}_2\text{S}$ ,  $\text{Li}_3\text{P}$ ,  $\gamma\text{-Li}_3\text{PS}_4$ , and  $\text{Li}_7\text{P}_3\text{S}_{11}$ . Since the behaviour of  $\text{Li}_3\text{P} // \text{Li}$  and  $\gamma\text{-Li}_3\text{PS}_4 // \text{Li}$  are very similar to that of  $\text{Li}_2\text{S} // \text{Li}$  and  $\text{Li}_7\text{P}_3\text{S}_{11} // \text{Li}$ , respectively, we will only focus on the latter two cases. The results for the former two cases can be found in **Supporting Information**. These simulations serve as a benchmark for understanding the behaviour of Li anode interfaces against the novel ternary systems. Operated at elevated temperatures of 525 K and 1075 K, our investigation is designed to delve into the stability dynamics of these interfaces, unravel the underlying chemical interactions at play, and discern the intricate formation mechanisms governing the SEI layers. We present the evolution of the systems at various time steps for 525 K in **Figure 7a and b**. The dashed black lines indicate the initial positions of the interfaces at the beginning of the simulation ( $t = 0$ ). Both the  $\text{Li}_2\text{S} // \text{Li}$  and  $\text{Li}_3\text{P} // \text{Li}$  interfaces preserve their original structures over time even at an elevated temperature of 1075 K. Conversely, at the  $\gamma\text{-Li}_3\text{PS}_4 // \text{Li}$  and  $\text{Li}_7\text{P}_3\text{S}_{11} // \text{Li}$  interfaces, diffusion of sulphur and phosphorus atoms into the lithium metal is observed, indicating instability akin to that at 0 K (i.e. geometry optimisations, see **Figure 6**). This instability intensifies and the degradation accelerates at higher temperatures.

The positional histograms (perpendicular to the interface – along the c-axis) for phosphorus and sulphur atoms, presented in **Figure 7c and d**, elucidate the instability of the  $\text{Li}_7\text{P}_3\text{S}_{11} // \text{Li}$  interfaces, while simultaneously demonstrating the structural integrity of the  $\text{Li}_2\text{S}$  framework. In this stable framework, the S atoms wobble around their initial positions, retaining their original peak position, shape, and height in the histogram. In contrast, the P and S atoms in the highly-conductive  $\text{Li}_7\text{P}_3\text{S}_{11}$  electrolyte become widely dispersed. A similar conclusion can be drawn from the pair distribution functions (PDF) for various atom pairs in these systems, as shown in **Figure 7e and f**. In  $\text{Li}_2\text{S} // \text{Li}$  system, the separation distances between Li-S and S-S pairs remain relatively unchanged over time. However, in  $\text{Li}_7\text{P}_3\text{S}_{11} // \text{Li}$  system, the initial peak diminishes due to the dissolution of  $\text{PS}_4$  tetrahedra at the interface, which decreases the number of P-S bonds.

**Figure 8a, b and c** illustrate the distribution of atomic coordination numbers for various atoms at different times, using a coordination radius of 3 Å. While there is no significant change in  $\text{Li}_2\text{S} // \text{Li}$  system, in  $\text{Li}_7\text{P}_3\text{S}_{11} // \text{Li}$  system, the coordination number with S atoms remains relatively stable, whereas it increases for P atoms. This is due to the aforementioned dissolution of  $\text{PS}_4$  units to form new Li-P bonds which increases the coordination number of P atoms from around 7 to 9.

To gain a deeper understanding of the microstructural changes, we further analysed the  $\text{Li}_7\text{P}_3\text{S}_{11} // \text{Li}$  system. Given the interface instability already at  $t = 20$  ps, the interface region was divided into two subregions, as shown in **Figure 8d**: the decomposing region, also referred to as the SEI layer, and the crystalline region, which resembles the  $\text{Li}_7\text{P}_3\text{S}_{11}$  crystal structure. Detailed examination of randomly-selected S and P atoms from these two regions reveals significant differences in their coordination. Notably, P atoms, which are initially surrounded by S atoms in the crystalline region, become solely coordinated by Li atoms in the decomposing region. The coordination numbers of Li for P and S atoms in the decomposing region correspond well with those in the bulk  $\text{Li}_2\text{S}$  and bulk  $\text{Li}_3\text{P}$ . Therefore, a  $\text{Li}_2\text{S}$ -like layer where P atoms occasionally substitute S atoms forms, as suggested by other studies.<sup>69,73-76</sup> With a much longer simulation on a much larger system, it might even be possible to observe the formation of

separate  $\text{Li}_2\text{S}$  and  $\text{Li}_3\text{P}$  regions. This is, however, limited by the high cost of AIMD simulations, calling for other approaches, like machine-learned interatomic potentials.

The decomposition reaction for the  $\gamma\text{-Li}_3\text{PS}_4$  and  $\text{Li}_7\text{P}_3\text{S}_{11}$  molecules are therefore as follows:



Here the reaction energies are calculated using the formation energies of the relevant species. These reactions result in a significant energy release due to the reduction of P atoms from  $5^+$  to  $3^-$ .

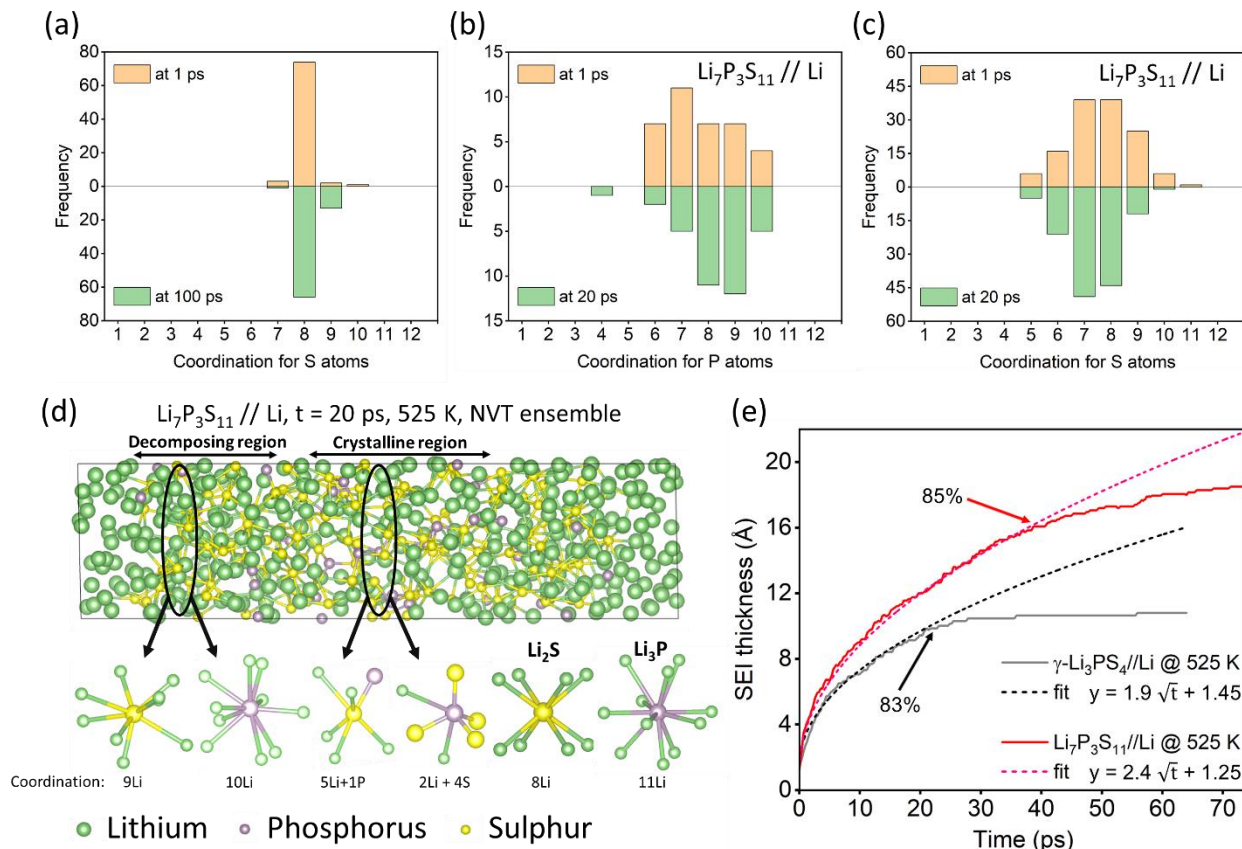


**Figure 8.** The coordination numbers a) for S atoms in  $\text{Li}_2\text{S} // \text{Li}$ , for b) P and c) S atoms in  $\text{Li}_7\text{P}_3\text{S}_{11} // \text{Li}$  interface structures. d) The microstructure of  $\text{Li}_7\text{P}_3\text{S}_{11} // \text{Li}$  system after 20 ps at 525 K. The microstructures around P and S atoms are also displayed for the interface region which is divided into two subregions: decomposing region (SEI layer) and crystalline region as well as bulk  $\text{Li}_2\text{S}$  and bulk  $\text{Li}_3\text{P}$  for comparison. e) The SEI layer thickness for  $\gamma\text{-Li}_3\text{PS}_4 // \text{Li}$  and  $\text{Li}_7\text{P}_3\text{S}_{11} // \text{Li}$  as a function of time at 525 K. A significant drop in the SEI growth rate is observed at 83% and 85% consumption of P and S atoms in the  $\text{Li}_3\text{PS}_4 // \text{Li}$  and  $\text{Li}_7\text{P}_3\text{S}_{11} // \text{Li}$  interface systems, respectively.

By analysing the microstructure at each time step, we derived an estimation of the SEI layer thickness as a function of time, as depicted in **Figure 8e**. Our model assumes that phosphorus and sulphur atoms coordinated solely with lithium atoms form  $\text{Li}_3\text{P}$ - and  $\text{Li}_2\text{S}$ -like structures, respectively. The SEI layer thickness was then calculated based on the relaxed bulk volumes of  $\text{Li}_3\text{P}$  and  $\text{Li}_2\text{S}$ . The analysis indicates that the initial structures, which are relaxed configurations at 0 K, already exhibit the presence of an SEI

layer. During the time evolution, SEI layer formation follows a square root dependence on time for both the  $\gamma$ -Li<sub>3</sub>PS<sub>4</sub>//Li and Li<sub>7</sub>P<sub>3</sub>S<sub>11</sub>//Li systems. After approximately 83–85% of the P and S atoms are consumed, the SEI growth rate decreases in both systems (**Figure 8e**). The observed square root dependence of SEI layer thickness on time may be attributed to the already formed SEI layer hindering further growth, while the subsequent deceleration is likely a consequence of simulation limitations, specifically the depletion of available P and S atoms necessary for continued SEI layer formation at the initial rate. The higher rate of SEI formation in the Li<sub>7</sub>P<sub>3</sub>S<sub>11</sub>//Li system compared to the  $\gamma$ -Li<sub>3</sub>PS<sub>4</sub>//Li system can be attributed to several factors. First,  $\gamma$ -Li<sub>3</sub>PS<sub>4</sub> is structurally more stable than Li<sub>7</sub>P<sub>3</sub>S<sub>11</sub> in its bulk form,<sup>70</sup> which may reduce the propensity for SEI formation in the former. Second, the microstructures at the interfaces differ between the two systems. It is important to note that even within the same material system, such as  $\gamma$ -Li<sub>3</sub>PS<sub>4</sub>//Li, the SEI formation rates can vary depending on the Miller indices of the interfaces. Third, the systems are subjected to different levels of strain, which could influence the SEI formation process. Finally, the mechanisms of SEI formation differ between the two systems: in the  $\gamma$ -Li<sub>3</sub>PS<sub>4</sub>//Li system, SEI formation is primarily driven by the dissolution of PS<sub>4</sub><sup>3-</sup> tetrahedral units, whereas in the Li<sub>7</sub>P<sub>3</sub>S<sub>11</sub>//Li system, both PS<sub>4</sub><sup>3-</sup> and P<sub>2</sub>S<sub>7</sub><sup>4-</sup> units contribute to the SEI layer formation.

### 3.4.2. Stability of novel Li-P-S compounds

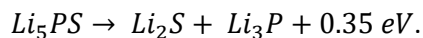
In this section, we examine the stability and SEI layer formation at the interfaces between novel ternary compounds (Li<sub>7</sub>PS<sub>2</sub>, Li<sub>5</sub>PS, Li<sub>8</sub>P<sub>2</sub>S, and Li<sub>11</sub>P<sub>3</sub>S) and lithium metal using AIMD simulations. Given that all the novel ternary-Li interfaces exhibit similar behaviour, we present the results for the system with the most conductive ternary, namely Li<sub>5</sub>PS // Li system, as a representative case and compare them with the benchmark interfaces, viz. Li<sub>2</sub>S // Li and Li<sub>7</sub>P<sub>3</sub>S<sub>11</sub>//Li. The results for other ternary compounds can be found in **Supporting Information**.

**Figure 9a** illustrates the structural evolution of the Li<sub>5</sub>PS // Li interface at 525 K. The dashed black lines represent the initial interface positions at the start of the simulation ( $t = 0$ ). Throughout the simulation, even at an elevated temperature of 1075 K, no migration of phosphorus or sulphur atoms is observed, indicating that the interfaces maintain their original structural integrity over time (unlike the  $\gamma$ -Li<sub>3</sub>PS<sub>4</sub> and Li<sub>7</sub>P<sub>3</sub>S<sub>11</sub> cases). Further evidence of the high stability is provided by the positional histogram shown in **Figure 9b**, which reveals that after 100 ps, the phosphorus and sulphur atoms remain very close to their initial positions without diffusing into the lithium metal, mirroring the behaviour observed in the Li<sub>2</sub>S // Li system. A similar conclusion is drawn from the PDFs for various atomic pairs, as presented in **Figure 9c**. The separation distances between Li-P, Li-S, and P-S pairs remain relatively constant, indicating stable atomic configurations over time.

To quantitatively assess the interface stability, the MSD of sulphur atoms across different systems is plotted in **Figure 9d**. As shown in the previous section, the instability of the  $\gamma$ -Li<sub>3</sub>PS<sub>4</sub>//Li and Li<sub>7</sub>P<sub>3</sub>S<sub>11</sub>//Li interfaces results in the diffusion of sulphur and phosphorus atoms into the lithium metal, leading to higher MSD values and elevated tracer diffusion coefficients. In both systems, the sulphur migration tends to decelerate after most of the sulphur atoms are consumed for SEI layer formation in a similar fashion to SEI layer growth shown in **Figure 8e**. In contrast, the sulphur atoms in the Li<sub>5</sub>PS // Li system exhibit mobility and a tracer diffusion coefficient comparable to that of the stable Li<sub>2</sub>S // Li system.

The coordination numbers for phosphorus and sulphur atoms within the Li<sub>5</sub>PS // Li system exhibit minimal variation over time (**Figure 9e and f**), further supporting the conclusion that the system remains stable. In **Figure 9g**, the microstructural environment surrounding the phosphorus and sulphur atoms in the Li<sub>5</sub>PS

layer is analyzed. A closer examination of individual phosphorus and sulphur atoms reveals that they are situated in Li<sub>3</sub>P-like and Li<sub>2</sub>S-like environments, respectively. This suggests that, unlike in the  $\gamma$ -Li<sub>3</sub>PS<sub>4</sub> and Li<sub>7</sub>P<sub>3</sub>S<sub>11</sub> cases (see **Figure 8d**), the phosphorus atoms in Li<sub>5</sub>PS (and other new Li<sub>2</sub>S-Li<sub>3</sub>P solid-solutions) are already in a 3<sup>-</sup> oxidation state, which diminishes the driving force for decomposition reactions. This observation is corroborated by the energetics of the corresponding decomposition reaction of Li<sub>5</sub>PS:



The energy gain from this reaction is negligible, approximately two orders of magnitude lower than that for Li<sub>7</sub>P<sub>3</sub>S<sub>11</sub>, further underscoring the thermodynamic stability of the Li<sub>5</sub>PS // Li interface.

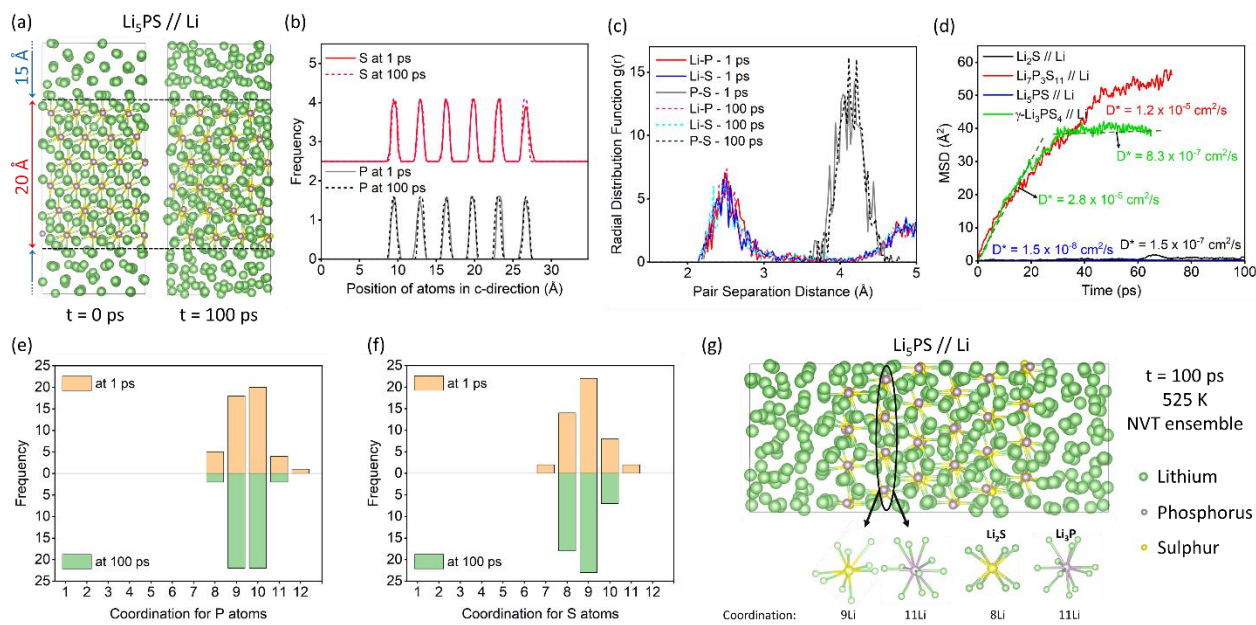


**Figure 9.** a) Evolution of the microstructure for the Li<sub>5</sub>PS // Li interface at 525 K. Black dashed lines indicate the positions of the initial interface in a); b) The positional histogram of P and S atoms along the c-axis (perpendicular to the interface). c) The pair distributions of selected atomic pairs. d) MSD for S atoms in Li<sub>2</sub>S // Li, Li<sub>7</sub>P<sub>3</sub>S<sub>11</sub> // Li, Li<sub>5</sub>PS // Li and  $\gamma$ -Li<sub>3</sub>PS<sub>4</sub> // Li interface systems. Calculated tracer diffusivities ( $D^*$ ) are also displayed. The coordination numbers for e) P atoms and f) S atoms in the Li<sub>5</sub>PS // Li interface structure. d) The microstructure of the Li<sub>5</sub>PS // Li system after 100 ps at 525 K. The microstructures around P and S atoms are also displayed alongside bulk Li<sub>2</sub>S and bulk Li<sub>3</sub>P for comparison.

### 3.5. Ionic diffusion of Li-P-S ternaries

In the previous section, we demonstrated that our novel ternary compounds exhibit stability against the lithium metal anode, similar to Li<sub>2</sub>S. However, Li<sub>2</sub>S is known for its notoriously low ionic diffusivity.<sup>59,60</sup> In this section, we investigate the diffusivity of Li-P-S ternary systems, with a particular emphasis on the impact of the interface on the diffusion properties.

**Figure 10** compares the AIMD lithium ion diffusion trajectories for bulk Li<sub>2</sub>S, Li<sub>7</sub>P<sub>3</sub>S<sub>11</sub>, and Li<sub>5</sub>PS systems, as well as their respective interfaces with lithium metal (Li<sub>2</sub>S // Li, Li<sub>7</sub>P<sub>3</sub>S<sub>11</sub> // Li, and Li<sub>5</sub>PS // Li). Li<sub>2</sub>S systems are depicted at an elevated temperature of 1075 K, as it exhibits negligible diffusion at 525 K. Although in

bulk Li<sub>2</sub>S, the Li atom migration still appears to be very limited even at 1075 K, T-O-T type diffusion pathways are clearly visible. In the Li<sub>2</sub>S // Li interface system, on the other hand, there is an increase in diffusion, likely due to the possibility of Li atom exchange between the electrolyte and the metal. However, the increase in diffusion in the bulk region is predominantly in the direction perpendicular to the interface, which limits its contribution to overall ionic conduction. In bulk Li<sub>7</sub>P<sub>3</sub>S<sub>11</sub>, well-defined (yet somewhat irregular) conduction pathways are observed, indicating a stable structural framework. Conversely, in the interface structure, these pathways are disrupted due to rapid interface degradation and SEI layer formation. Notably, the formation of this SEI layer impedes the movement of lithium ions which is visible as a grid-like pattern on the left side. Li<sub>5</sub>PS exhibits both high structural stability and high ionic conductivity, leading to a well-defined and similar ionic diffusion network in both bulk Li<sub>5</sub>PS and Li<sub>5</sub>PS // Li interface systems. The diffusion is three-dimensional and continues seamlessly (percolated) across the interface.

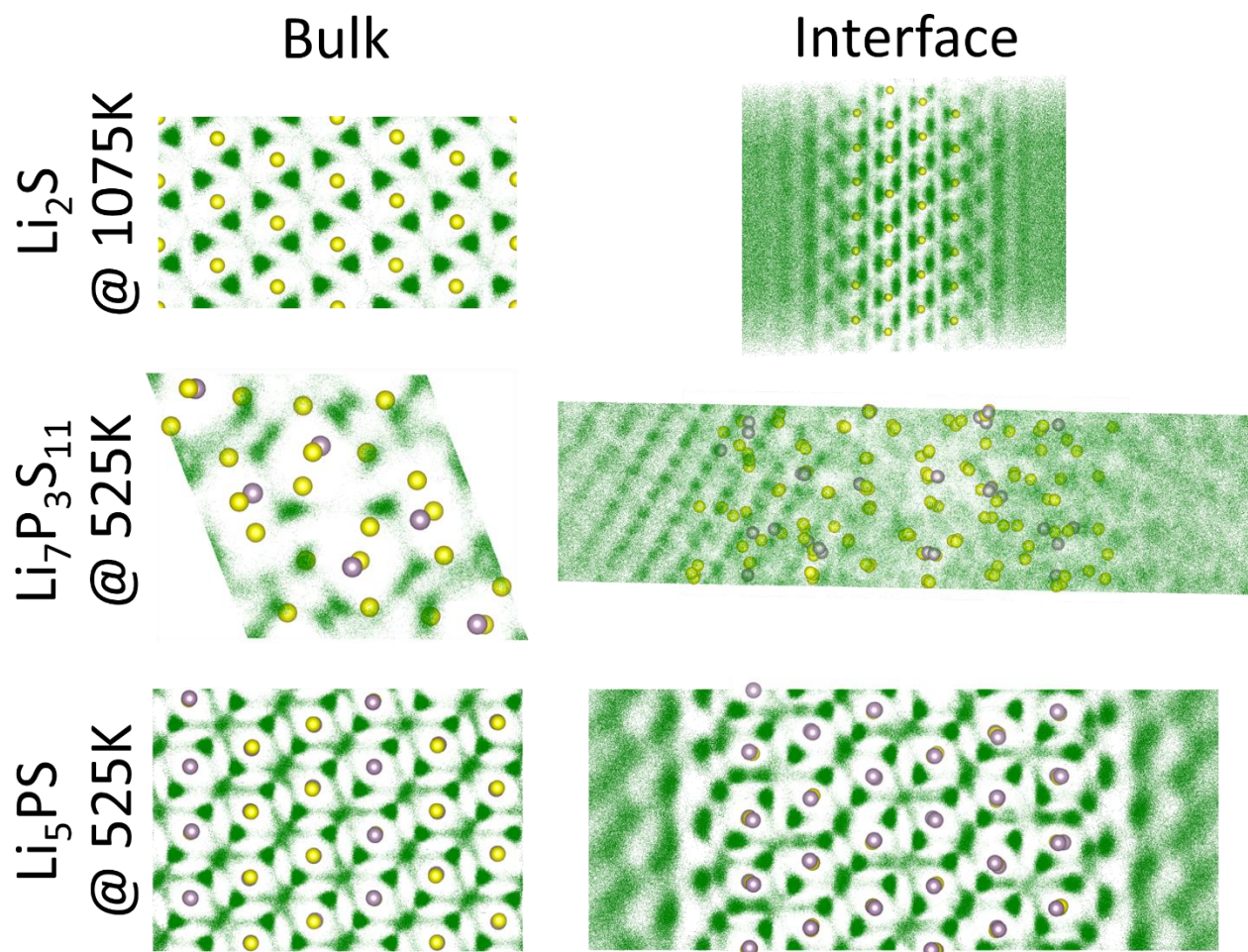


**Figure 10.** Li<sup>+</sup>-ion trajectory (green) for bulk Li<sub>2</sub>S, bulk Li<sub>7</sub>P<sub>3</sub>S<sub>11</sub>, and bulk Li<sub>5</sub>PS systems, as well as their respective interfaces with lithium metal (Li<sub>2</sub>S // Li, Li<sub>7</sub>P<sub>3</sub>S<sub>11</sub> // Li, and Li<sub>5</sub>PS // Li). Li<sub>7</sub>P<sub>3</sub>S<sub>11</sub> and Li<sub>5</sub>PS systems are presented at 525 K but Li<sub>2</sub>S systems are depicted at an elevated temperature of 1075 K, due to negligible diffusion at 525 K. The initial positions of the phosphorus (purple) and sulphur (yellow) atoms (at t = 0 ps) are shown in the background. Similar Li-ion trajectory plots for other bulk and interface systems can be found in **Supporting Information, Figure S8**.

### 3.5.1. Van Hove correlation of Li<sup>+</sup>-ions in bulk and interface systems

Van Hove correlation function is a crucial analytical tool for probing the microscopic dynamics of ion transport within solid and liquid electrolytes. By decomposing the Van Hove function into its self and distinct components, ion mobility and interactions over time can be studied to understand ionic conductivity and diffusion mechanisms.

Consider a system of  $N$  particles, specifically Li atoms, with time-dependent position coordinates  $\mathbf{r}_i(t)$ , where  $i = 1, \dots, N$  represents the particle index, and  $t$  denotes time. The Van Hove correlation function is defined as the probability of finding a particle at position  $\mathbf{r}$  at time  $t$ , given that a particle was located at the origin at  $t = 0$ :

$$G(r, t) = \frac{1}{N} \langle \sum_{i=1}^N \sum_{j=1}^N \delta(\mathbf{r} + \mathbf{r}_j(0) - \mathbf{r}_i(t)) \rangle, \quad (12)$$

where  $\langle \dots \rangle$  denotes an ensemble average and  $\delta$  is the three-dimensional Dirac delta function. The function  $G(r, t)$  can be decomposed into two components, conventionally termed the "self" part and the "distinct" part, by distinguishing between the cases  $i = j$  and  $i \neq j$ , respectively:

$$G(r, t) = G_s(r, t) + G_d(r, t) = \frac{1}{N} \langle \sum_{i=1}^N \delta(\mathbf{r} + \mathbf{r}_i(0) - \mathbf{r}_i(t)) \rangle + \frac{1}{N} \langle \sum_{i \neq j}^N \delta(\mathbf{r} + \mathbf{r}_j(0) - \mathbf{r}_i(t)) \rangle. \quad (13)$$

For a given  $r$  and  $t$ , the self-part  $G_s(r, t)$  quantifies the likelihood that a particle has moved from its initial position by a distance  $r$  after a time interval  $t$ . Conversely, the distinct part  $G_d(r, t)$  describes the radial distribution of the remaining  $N - 1$  particles relative to the initial reference particle at time  $t$ . Notably,  $G_d(r, t)$  reduces to the static pair distribution function when  $t = 0$ , which is frequently used to analyse the dynamics of structural changes in the system.

**Figure 11** presents the distinct part of the Van Hove correlation function  $G_d(r, t)$  for Li<sub>2</sub>S, Li<sub>7</sub>P<sub>3</sub>S<sub>11</sub>, and Li<sub>5</sub>PS systems. For bulk Li<sub>2</sub>S at 525 K, the lack of observed lithium diffusion results in a plot that closely resembles the radial distribution function (RDF) over time, exhibiting the first and second coordination shells at approximately 3 Å and 4 Å, respectively. However, at the elevated temperature of 1075 K, the lithium atoms in Li<sub>2</sub>S acquire sufficient energy to diffuse, leading to a pronounced peak in  $G_d(r, t)$  near  $r = 0$ , indicating highly correlated Li<sup>+</sup>-ion motions and a high probability that a vacated Li site is quickly occupied by another Li atom. A similar behaviour is observed in bulk Li<sub>7</sub>P<sub>3</sub>S<sub>11</sub>, bulk Li<sub>5</sub>PS, and Li<sub>5</sub>PS // Li systems at 525 K. In Li<sub>7</sub>P<sub>3</sub>S<sub>11</sub> // Li system, however, the peak near  $r = 0$  is weak and diffuse. This can be attributed to degradation at the interface and the formation of the SEI layer, which disrupts the well-defined initial Li occupation sites. Additionally, the coordination shells in both bulk Li<sub>7</sub>P<sub>3</sub>S<sub>11</sub> and Li<sub>7</sub>P<sub>3</sub>S<sub>11</sub> // Li systems appear less distinct. In contrast, both bulk Li<sub>5</sub>PS and Li<sub>5</sub>PS // Li systems exhibit pronounced peaks near  $r = 0$  and well-defined coordination shells due to high stability and diffusivity as discussed in previous sections.

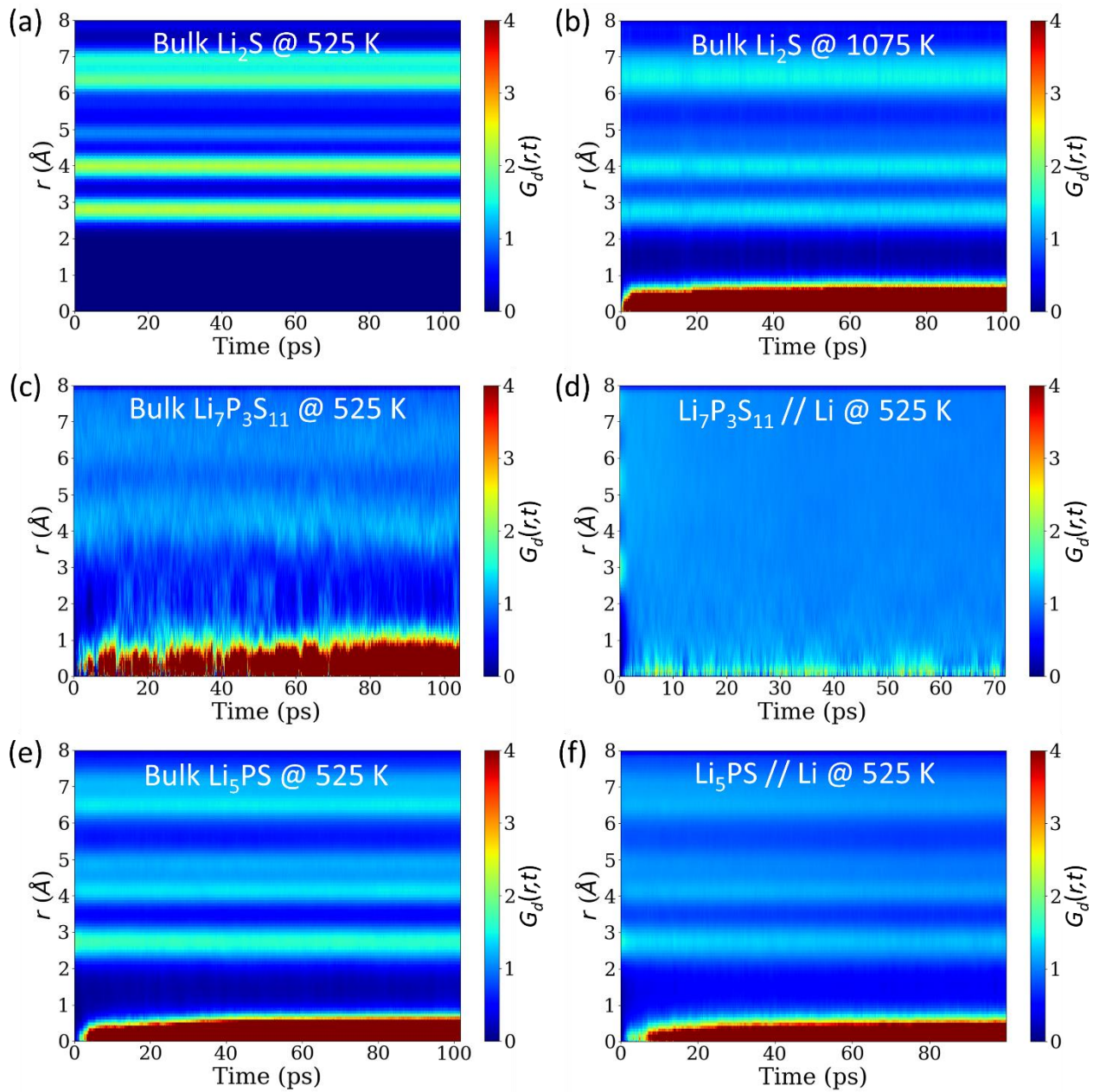


**Figure 11.** The distinct part of the Van Hove correlation function for Li atoms in a) bulk  $\text{Li}_2\text{S}$  at 525 K, b) bulk  $\text{Li}_2\text{S}$  at 1075 K, c) bulk  $\text{Li}_7\text{P}_3\text{S}_{11}$  at 525 K, d)  $\text{Li}_7\text{P}_3\text{S}_{11} // \text{Li}$  at 525 K, e)  $\text{Li}_5\text{PS}$  at 525 K and, f)  $\text{Li}_5\text{PS} // \text{Li}$  at 525 K. Similar Van Hove correlation plots for other bulk and interface systems can be found in **Supporting Information, Figure S9**.

### 3.5.2. Diffusion at the interface

To investigate the nanoscale diffusion properties of electrolytes, particularly at their interfaces with Li metal, we developed a Python code that tracks the number of  $\text{Li}^+$ -ions crossing an imaginary membrane, as illustrated in **Figure 12a**, in both directions perpendicular to the interface (along the c-axis). The c-axis in the bulk systems are aligned with specific Miller indices to ensure the same orientation as in the interface structure. The membrane thickness is set to 3 Å to avoid counting oscillatory motions of  $\text{Li}^+$ -ions

at a single site, which do not represent actual site-to-site jumps. To examine the impact of interfacing the electrolyte with lithium metal anode, the membrane is positioned within the bulk electrolyte (referred to as "bulk"), at the interface (referred to as "interface"), and at the centre (referred to as "centre") of the electrolyte in the interface system. We note that these diffusion events are sampled at thermodynamic equilibrium/steady-state, as the AIMD simulations do not entail a background electric field applied on the ions, as opposed to the real-life charging/discharging process.

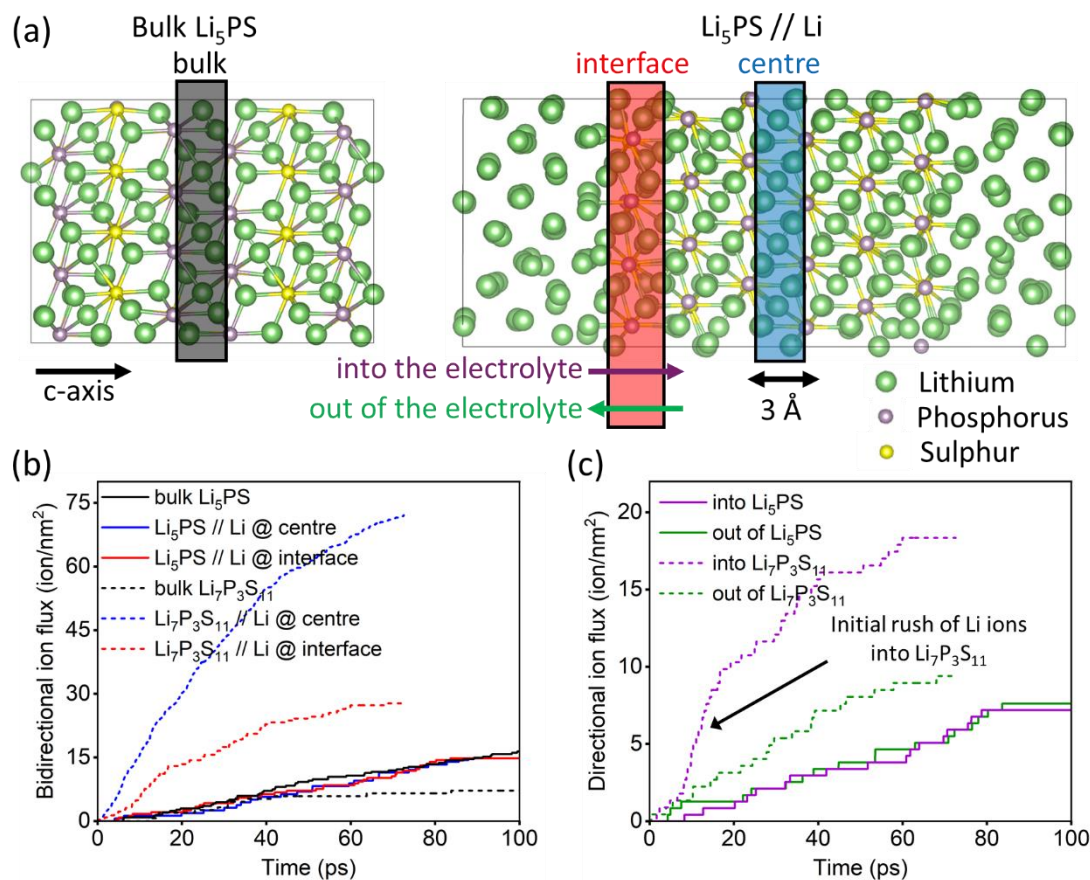


**Figure 12.** Local diffusion calculations for  $\text{Li}^+$ -ions. a) The imaginary membranes used to calculate the flux of ions are depicted in bulk  $\text{Li}_5\text{PS}$  and  $\text{Li}_5\text{PS} // \text{Li}$  interface structures for bulk region (black), interface region (red) and centre of the electrolyte (blue). b) Bidirectional ion flux through bulk, interface and centre regions for bulk  $\text{Li}_5\text{PS}$  and  $\text{Li}_7\text{P}_3\text{S}_{11}$  along with  $\text{Li}_5\text{PS} // \text{Li}$  and  $\text{Li}_7\text{P}_3\text{S}_{11} // \text{Li}$  interface systems. c) Directional flux into and out of the electrolyte calculated using the  $\text{Li}_5\text{PS} // \text{Li}$  and  $\text{Li}_7\text{P}_3\text{S}_{11} // \text{Li}$  interface models.

In **Figure 12b**, we compare the total bidirectional flux of  $\text{Li}^+$ -ions for bulk  $\text{Li}_5\text{PS}$  and bulk  $\text{Li}_7\text{P}_3\text{S}_{11}$ , as well as their interfaces with the lithium metal anode at 525 K. For  $\text{Li}_5\text{PS}$ , the flux at both the "centre" and "interface" regions of the interface system is very similar to that observed in the "bulk" region, with a constant increase in flux over time across all regions. This indicates the absence of significant internal resistance to  $\text{Li}^+$ -ion flux at the interface. In contrast, for  $\text{Li}_7\text{P}_3\text{S}_{11}$ , the flux at the "interface" is lower than that at the "centre", suggesting the presence of resistance, likely due to the formation of the SEI layer that impedes  $\text{Li}^+$ -ion flux. However, the fluxes at both the "interface" and "centre" are significantly higher than

in the "bulk," indicating the presence of a different diffusion mechanism in the  $\text{Li}_7\text{P}_3\text{S}_{11}$  // Li system than its bulk counterpart.

**Figure 12c** presents the  $\text{Li}^+$ -ion flux into and out of the electrolytes in  $\text{Li}_5\text{PS}$  // Li and  $\text{Li}_7\text{P}_3\text{S}_{11}$  // Li systems at 525 K. Initially, the slope of the  $\text{Li}^+$ -ion flux into the electrolyte is much steeper than the flux out, indicating a rapid influx of Li atoms into the electrolyte in  $\text{Li}_7\text{P}_3\text{S}_{11}$  // Li system. After 40 ps, the slopes of the fluxes in each direction become similar, suggesting a steady state. The initial surge of Li ions into the electrolyte is attributed to the porous nature of the material. In bulk  $\text{Li}_7\text{P}_3\text{S}_{11}$ , ionic conduction occurs via Li ion jumps from one site to another. However, when  $\text{Li}_7\text{P}_3\text{S}_{11}$  is interfaced with the Li metal, the excess Li atoms rapidly infiltrate the pores of  $\text{Li}_7\text{P}_3\text{S}_{11}$ , not only leading to the formation of an SEI layer but also providing an alternative conduction pathway through vacant interstitial sites, leading to a change in the principle conduction mechanism. In contrast, the structural framework of  $\text{Li}_5\text{PS}$  is robust, and conduction mainly occurs through stable vacant interstitial sites, as discussed in **Section 3.1**. Consequently, the flux of Li ions through the interface is balanced in both directions and the steady-state is observed throughout the simulation.

#### 4. Conclusion

Our comprehensive DFT simulations have revealed the diffusion mechanisms and the underlying reasons for the high ionic conductivity in novel Li-P-S ternary electrolytes,  $\text{Li}_7\text{PS}_2$ ,  $\text{Li}_5\text{PS}$ ,  $\text{Li}_8\text{P}_2\text{S}$ , and  $\text{Li}_{11}\text{P}_3\text{S}$ . These materials, exhibiting ionic conductivities on par with the well-known highly-conductive  $\text{Li}_7\text{P}_3\text{S}_{11}$ , represent a promising class of electrolytes for solid-state batteries. Among the newly studied ternaries,  $\text{Li}_5\text{PS}$  stands out with the highest conductivity, a property we attribute to the homogenous distribution of phosphorus and sulphur atoms within its structure (due to the 1:1 P to S ratio). This balanced atomic arrangement facilitates more efficient lithium-ion transport, reducing energy barriers and enabling faster ionic movement through the lattice.

Our investigation also extended to the thermodynamic stability of these ternaries in contact with lithium metal anodes, a crucial factor for practical Li-metal battery applications. Unlike  $\text{Li}_7\text{P}_3\text{S}_{11}$ , which rapidly forms a SEI layer due to the reduction of phosphorus from an oxidation state of 5<sup>+</sup> to 3<sup>-</sup>, the novel Li-P-S ternaries demonstrate remarkable stability. The SEI formation rate in  $\text{Li}_7\text{P}_3\text{S}_{11}$  is a time-dependent process, where the thickness of the interphase layer grows proportionally to the square root of time, progressively increasing the internal resistance and reducing the battery's overall efficiency. The stability of novel ternaries is rooted in their unique  $\text{Li}_2\text{S}$ -like structural framework, which inherently positions phosphorus atoms in the 3<sup>-</sup> oxidation state, thereby eliminating the main (chemical) driving force for SEI formation. The absence of SEI layer is particularly significant, as it means that no additional resistance is introduced at the electrolyte-anode interface, which is a common issue in many solid-state battery systems. These findings not only highlight the suitability of novel ternaries as high-performance solid electrolytes but also underscore the importance of structural design in developing next-generation battery materials. By avoiding the issues associated with SEI formation, the novel Li-P-S ternaries can maintain high ionic conductivity and stability over extended periods, making them ideal candidates as electrolytes and coating materials for use in solid-state lithium batteries.

In summary, our study provides a detailed understanding of the physical mechanisms driving the superior performance of these new Li-P-S ternary electrolytes. The insights gained from our work pave the way for

the development of advanced solid-state batteries that combine high ionic conductivity with robust chemical and electrochemical stability. These findings suggest that the novel ternaries, particularly Li<sub>5</sub>PS, could play a crucial role in the future of energy storage technologies, offering a pathway to safer, more efficient, and longer-lasting batteries.

## 5. Acknowledgements

B.K. and H.S.S. acknowledge support from the UK Engineering and Physical Sciences Research Council (EPSRC) through the Early Career Fellowship (EP/T026138/1). Computing facilities were provided by the Scientific Computing Research Technology Platform (SC-RTP) at the University of Warwick. DFT calculations were performed using the Avon and Sulis HPC platforms, and Sulis is funded by the EPSRC Grant EP/T022108/1 and the HPC Midlands+ consortium. This work also used the ARCHER2 UK National Supercomputing Service (<https://www.archer2.ac.uk>) for performing the DFT calculations (through the Project e848).

## 6. References

1. Xuning Feng, Dongsheng Ren, Xiangming He, and Minggao Ouyang, Mitigating Thermal Runaway of Lithium-Ion Batteries, Joule, 4, 743–770, 2020
2. Zeyu Chen, Rui Xiong, Jiahuan Lu, Xinggang Li, Temperature rise prediction of lithium-ion battery suffering external short circuit for all-climate electric vehicles application, Applied Energy, 2018, 213, 375-383
3. Donal P. Finegan, Mario Scheel, James B. Robinson, Bernhard Tjaden, Ian Hunt, Thomas J. Mason, Jason Millichamp, Marco Di Michiel, Gregory J. Offer, Gareth Hinds, Dan J.L. Brett, Paul R. Shearing, In-operando high-speed tomography of lithium-ion batteries during thermal runaway, Nature Communications volume 6, Article number: 6924 (2015)
4. T. Krauskopf, F. H. Richter, W. G. Zeier and J. Janek, Physicochemical concepts of the lithium metal anode in solid-state batteries, Chem. Rev., 2020, 120(15), 7745–7794..
5. X.-B. Cheng, R. Zhang, C.-Z. Zhao and Q. Zhang, Toward Safe Lithium Metal Anode in Rechargeable Batteries: A Review Chem. Rev., 2017, 117, 10403–10473.
6. C. Fang, B. Lu, G. Pawar, M. Zhang, D. Cheng, S. Chen, M. Ceja, J.-M. Doux, H. Musrock, M. Cai, B. Liaw and Y. S. Meng, Pressure-tailored lithium deposition and dissolution in lithium metal batteries, Nat. Energy, 2021, 6, 987–994.
7. Xiao Liang, Quan Pang, Ivan R. Kochetkov, Marina Safont Sempere, He Huang, Xiaoqi Sun & Linda F. Nazar, A facile surface chemistry route to a stabilized lithium metal anode. *Nat Energy* 2, 17119 (2017).
8. Lin, D., Liu, Y. & Cui, Y. Reviving the lithium metal anode for high-energy batteries. *Nat. Nanotechnol.* 12, 194–206 (2017).
9. P. Xue, S. Liu, X. Shi, C. Sun, C. Lai, Y. Zhou, D. Sui, Y. Chen, J. Liang, A hierarchical silver-nanowire-graphene host enabling ultrahigh rates and superior long-term cycling of lithium-metal composite anodes. *Adv. Mater.* 30, 1804165 (2018).
10. Cheng Xin-Bing, Zhang R., Zhao Chen-Zi, Wei F., Zhang Ji-Guang, Zhang Q. A Review of Solid Electrolyte Interphases on Lithium Metal Anode. *Adv. Sci.*, (2016) 3: 1500213.

11. Wu Xu, Jiulin Wang, Fei Ding, Xilin Chen, Eduard Nasybulin, Yaohui Zhangad and Ji-Guang Zhang, Lithium metal anodes for rechargeable batteries, *Energy Environ. Sci.*, 2014, 7, 513–537.
12. P. Albertus, S. Babinec, S. Litzelman, A. Newman, Status and challenges in enabling the lithium metal electrode for high-energy and low-cost rechargeable batteries, *Nat. Energy* 2018, 3, 16–21.
13. Ohta, N.; Takada, K.; Zhang, L.; Ma, R.; Osada, M.; Sasaki, T. Enhancement of the High-Rate Capability of Solid-State Lithium Batteries by Nanoscale Interfacial Modification. *Adv. Mater.* 2006, 18, 2226–2229.
14. Takada, K.; Inada, T.; Kajiyama, A.; Sasaki, H.; Kondo, S.; Watanabe, M.; Murayama, M.; Kanno, R. Solid-State Lithium Battery with Graphite Anode. *Solid State Ionics* 2003, 158, 269–274.
15. Lin, L.; Liang, F.; Zhang, K.; Mao, H.; Yang, J.; Qian, Y. Lithium Phosphide/Lithium Chloride Coating on Lithium for Advanced Lithium Metal Anode. *J. Mater. Chem. A* 2018, 6, 15859–15867.
16. Lalère, F.; Leriche, J. B.; Courty, M.; Boulineau, S.; Viallet, V.; Masquelier, C.; Seznec, V. An All-Solid State NASICON Sodium Battery Operating at 200 °C. *J. Power Sources* 2014, 247, 975–980.
17. Kitaura, H.; Zhou, H. All-Solid-State Lithium-Oxygen Battery with High Safety in Wide Ambient Temperature Range. *Sci. Rep.* 2015, 5, 13271.
18. Janek, J.; Zeier, W. G. A Solid Future for Battery Development. *Nat. Energy* 2016, 1, 16141.
19. Murugan, R.; Thangadurai, V.; Weppner, W. Fast Lithium Ion Conduction in Garnet-Type Li<sub>7</sub>La<sub>3</sub>Zr<sub>2</sub>O<sub>12</sub>. *Angew. Chem., Int. Ed.* 2007, 46, 7778–7781.
20. Knauth, P. Inorganic Solid Li Ion Conductors: An Overview. *Solid State Ionics* 2009, 180, 911–916.
21. Bachman, J. C.; Muy, S.; Grimaud, A.; Chang, H.-H.; Pour, N.; Lux, S. F.; Paschos, O.; Maglia, F.; Lupart, S.; Lamp, P.; Giordano, L.; Shao-Horn, Y. Inorganic Solid-State Electrolytes for Lithium Batteries: Mechanisms and Properties Governing Ion Conduction. *Chem. Rev.* 2016, 116, 140–162.
22. Dietrich, C.; Weber, D. A.; Sedlmaier, S. J.; Indris, S.; Culver, S. P.; Walter, D.; Janek, J.; Zeier, W. G. Lithium Ion Conductivity in Li<sub>2</sub>S-P<sub>2</sub>S<sub>5</sub> glasses-Building Units and Local Structure Evolution during the Crystallization of Superionic Conductors Li<sub>3</sub>PS<sub>4</sub>, Li<sub>7</sub>P<sub>3</sub>S<sub>11</sub>and Li<sub>4</sub>P<sub>2</sub>S<sub>7</sub>. *J. Mater. Chem. A* 2017, 5, 18111–18119.
23. Berbano, S. S.; Mirsaneh, M.; Lanagan, M. T.; Randall, C. A. Lithium Thiophosphate Glasses and Glass–Ceramics as Solid Electrolytes: Processing, Microstructure, and Properties. *Int. J. Appl. Glass Sci.* 2013, 4, 414–425.
24. Kamaya, N.; Homma, K.; Yamakawa, Y.; Hirayama, M.; Kanno, R.; Yonemura, M.; Kamiyama, T.; Kato, Y.; Hama, S.; Kawamoto, K.; Mitsui, A. A Lithium Superionic Conductor. *Nat. Mater.* 2011, 10, 682–686.
25. Patel, S. V.; Banerjee, S.; Liu, H.; Wang, P.; Chien, P.-H.; Feng, X.; Liu, J.; Ong, S. P.; Hu, Y.-Y. Tunable Lithium-Ion Transport in Mixed-Halide Argyrodites Li<sub>6</sub>–XPS<sub>5</sub>–XCIBRx: An Unusual Compositional Space. *Chem. Mater.* 2021, 33, 1435–1443.
26. Kato, Y.; Hori, S.; Saito, T.; Suzuki, K.; Hirayama, M.; Mitsui, A.; Yonemura, M.; Iba, H.; Kanno, R. High-Power All-Solid-State Batteries Using Sulfide Superionic Conductors. *Nat. Energy* 2016, 1, 16030.
27. Strangmüller, S.; Eickhoff, H.; Müller, D.; Klein, W.; Raudaschl-Sieber, G.; Kirchhain, H.; Sedlmeier, C.; Baran, V.; Senyshyn, A.; Deringer, V. L.; van Wüllen, L.; Gasteiger, H. A.; Fassler, T. F. Fast Ionic Conductivity in the Most Lithium-Rich Phosphidosilicate Li<sub>14</sub>SiP<sub>6</sub>. *J. Am. Chem. Soc.* 2019, 141, 14200–14209.

28. Restle, T. M. F.; Sedlmeier, C.; Kirchhain, H.; Klein, W.; Raudaschl-Sieber, G.; Deringer, V. L.; van Wüllen, L.; Gasteiger, H. A.; Fassler, T. F. Fast Lithium Ion Conduction in Lithium Phosphidoaluminates. *Angew. Chem., Int. Ed.* 2020, 59, 5665–5674.
29. Strangmüller, S.; Eickhoff, H.; Raudaschl-Sieber, G.; Kirchhain, H.; Sedlmeier, C.; van Wüllen, L.; Gasteiger, H. A.; Fassler, T. F. Modifying the Properties of Fast Lithium-Ion Conductors\_The Lithium Phosphidotetrelates Li<sub>14</sub>SiP<sub>6</sub>, Li<sub>14</sub>GeP<sub>6</sub>, and Li<sub>14</sub>SnP<sub>6</sub>. *Chem. Mater.* 2020, 32, 6925–6934.
30. Restle, T. M. F.; Sedlmeier, C.; Kirchhain, H.; Klein, W.; Raudaschl-Sieber, G.; van Wüllen, L.; Fassler, T. F. Fast Lithium-Ion Conduction in Phosphide Li<sub>9</sub>GaP<sub>4</sub>. *Chem. Mater.* 2021, 33, 2957–2966.
31. Toffoletti, L.; Kirchhain, H.; Landesfeind, J.; Klein, W.; van Wüllen, L.; Gasteiger, H. A.; Fassler, T. F. Lithium Ion Mobility in Lithium Phosphidosilicates: Crystal Structure, <sup>7</sup>Li, <sup>29</sup>Si, and <sup>31</sup>P MAS NMR Spectroscopy, and Impedance Spectroscopy of Li<sub>8</sub>SiP<sub>4</sub> and Li<sub>2</sub>SiP<sub>2</sub>. *Chem.\_Eur. J.* 2016, 22, 17635–17645.
32. Eickhoff, H.; Strangmüller, S.; Klein, W.; Kirchhain, H.; Dietrich, C.; Zeier, W. G.; van Wüllen, L.; Fassler, T. F. Lithium Phosphidogermanates  $\alpha$ - and  $\beta$ -Li<sub>8</sub>GeP<sub>4</sub>\_A Novel Compound Class with Mixed Li<sup>+</sup> Ionic and Electronic Conductivity. *Chem. Mater.* 2018, 30, 6440–6448.
33. Strangmüller, S.; Eickhoff, H.; Klein, W.; Raudaschl-Sieber, G.; Kirchhain, H.; Kutsch, T.; Baran, V.; Senyshyn, A.; van Wüllen, L.; Gasteiger, H. A.; Fassler, T. F. Synthesis, Structure and Diffusion Pathways of Fast Lithium-Ion Conductors in the Polymorphs  $\alpha$ - and  $\beta$ -Li<sub>8</sub>SnP<sub>4</sub>. *J. Mater. Chem. A* 2021, 9, 15254–15268.
34. Richards, W. D.; Miara, L. J.; Wang, Y.; Kim, J. C.; Ceder, G. Interface Stability in Solid-State Batteries. *Chem. Mater.* 2016, 28, 266–273.
35. Han, F.; Zhu, Y.; He, X.; Mo, Y.; Wang, C. Electrochemical Stability of Li<sub>10</sub>GeP<sub>2</sub>S<sub>12</sub> and Li<sub>7</sub>La<sub>3</sub>Zr<sub>2</sub>O<sub>12</sub> Solid Electrolytes. *Adv. Energy Mater.* 2016, 6, 1501590.
36. Ong, S. P.; Mo, Y.; Richards, W. D.; Miara, L.; Lee, H. S.; Ceder, G. Phase Stability, Electrochemical Stability and Ionic Conductivity of the Li<sub>10</sub>□<sub>1</sub>MP<sub>2</sub>X<sub>12</sub> (M = Ge, Si, Sn, Al or P, and X = O, S or Se) Family of Superionic Conductors. *Energy Environ. Sci.* 2012, 6, 148–156.
37. Zhu, Y.; He, X.; Mo, Y. Strategies Based on Nitride Materials Chemistry to Stabilize Li Metal Anode. *Adv. Sci.* 2017, 4, 1600517.
38. Wenzel, S.; Randau, S.; Leichtweis, T.; Weber, D. A.; Sann, J.; Zeier, W. G.; Janek, J. Direct Observation of the Interfacial Instability of the Fast Ionic Conductor Li<sub>10</sub>GeP<sub>2</sub>S<sub>12</sub> at the Lithium Metal Anode. *Chem. Mater.* 2016, 28, 2400–2407.
39. Harper, A. F.; Evans, M. L.; Darby, J. P.; Karasulu, B.; Koçer, C. P.; Nelson, J. R.; Morris, A. J. Ab Initio Structure Prediction Methods for Battery Materials : A Review of Recent Computational Efforts to Predict the Atomic Level Structure and Bonding in Materials for Rechargeable Batteries. *Johns. Matthey Technol. Rev.* 2020, 64, 103–118.
40. Wang, Y.; Richards, W. D.; Ong, S. P.; Miara, L. J.; Kim, J. C.; Mo, Y.; Ceder, G. Design Principles for Solid-State Lithium Superionic Conductors. *Nat. Mater.* 2015, 14, 1026–1031.
41. Van der Ven, A.; Deng, Z.; Banerjee, S.; Ong, S. P. Rechargeable Alkali-Ion Battery Materials: Theory and Computation. *Chem. Rev.* 2020, 120, 6977–7019.
42. Pasta, M.; Armstrong, D.; Brown, Z. L.; Bu, J.; Castell, M. R.; Chen, P.; Cocks, A.; Corr, S. A.; Cussen, E. J.; Darnbrough, E.; Deshpande, V.; Doerrer, C.; Dyer, M. S.; El-Shinawi, H.; Fleck, N.; Grant, P.; Gregory,

- G. L.; Grovenor, C.; Hardwick, L. J.; Irvine, J. T. S.; Lee, H. J.; Li, G.; Liberti, E.; McClelland, I.; Monroe, C.; Nellist, P. D.; Shearing, P. R.; Shoko, E.; Song, W.; Jolly, D. S.; Thomas, C. I.; Turrell, S. J.; Vestli, M.; Williams, C. K.; Zhou, Y.; Bruce, P. G. Roadmap on Solid-State Batteries. *J. Phys. Energy* 2020, 2, 032008.
43. Oganov, A. R.; Pickard, C. J.; Zhu, Q.; Needs, R. J. Structure Prediction Drives Materials Discovery. *Nat. Rev. Mater.* 2019, 4, 331–348.
44. Zhu, Z.; Chu, I.-H.; Ong, S. P. Li<sub>3</sub>Y(PS<sub>4</sub>)<sub>2</sub> and Li<sub>5</sub>PS<sub>4</sub>Cl<sub>2</sub>: New Lithium Superionic Conductors Predicted from Silver Thiophosphates Using Efficiently Tiered Ab Initio Molecular Dynamics Simulations. *Chem. Mater.* 2017, 29, 2474–2484.
45. Prasada Rao, R.; Chen, H.; Adams, S. Stable Lithium Ion Conducting Thiophosphate Solid Electrolytes Li<sub>x</sub>(PS<sub>4</sub>)YX<sub>z</sub> (X = Cl, Br, I). *Chem. Mater.* 2019, 31, 8649–8662.
46. Dietrich, C.; Weber, D. A.; Sedlmaier, S. J.; Indris, S.; Culver, S. P.; Walter, D.; Janek, J.; Zeier, W. G. Lithium Ion Conductivity in Li<sub>2</sub>S–P<sub>2</sub>S<sub>5</sub> Glasses – Building Units and Local Structure Evolution during the Crystallization of Superionic Conductors Li<sub>3</sub>PS<sub>4</sub>, Li<sub>7</sub>P<sub>3</sub>S<sub>11</sub> and Li<sub>4</sub>P<sub>2</sub>S<sub>7</sub>. *J. Mater. Chem. A* 2017, 5, 18111–18119.
47. Conrad Szczuka, Bora Karasulu, Matthias F. Groh, Farheen N. Sayed, Timothy J. Sherman, Joshua D. Bocarsly, Sundeep Vema, Svetlana Menkin, Steffen P. Emge, Andrew J. Morris, and Clare P. Grey, Forced Disorder in the Solid Solution Li<sub>3</sub>P–Li<sub>2</sub>S: A New Class of Fully Reduced Solid Electrolytes for Lithium Metal Anodes, *Journal of the American Chemical Society* 2022 144 (36)
48. *INTERFCAER*: A Python-script for automated generation of atomistic models for solid-solid interfaces. Freely available under GNU license at <https://github.com/bkarasulu/INTERFACER-code>.
49. Kresse, G.; Hafner, J. Ab Initio Molecular Dynamics for Liquid Metals. *Phys. Rev. B* 1993, 47 (1), 558–561.
50. Kresse, G.; Furthmüller, J. Efficiency of Ab-Initio Total Energy Calculations for Metals and Semiconductors Using a Plane-Wave Basis Set. *Comput. Mater. Sci.* 1996, 6 (1), 15–50.
51. Kresse, G. Efficient Iterative Schemes for Ab Initio Total-Energy Calculations Using a Plane-Wave Basis Set. *Phys. Rev. B* 1996, 54 (16), 11169–11186.
52. Blöchl, P. E. Projector Augmented-Wave Method. *Phys. Rev. B* 1994, 50 (24), 17953–17979.
53. Kresse, G. From Ultrasoft Pseudopotentials to the Projector Augmented-Wave Method. *Phys. Rev. B* 1999, 59 (3), 1758–1775.
54. Perdew, J. P.; Yue, W. Accurate and Simple Density Functional for the Electronic Exchange Energy: Generalized Gradient Approximation. *Phys. Rev. B* 1986, 33 (12), 8800–8802.
55. Momma, K.; Izumi, F. VESTA 3 for Three-Dimensional Visualization of Crystal, Volumetric and Morphology Data. *J. Appl. Crystallogr.* 2011, 44, 1272–1276.
56. A. Stukowski, Visualization and analysis of atomistic simulation data with OVITO - the Open Visualization Tool, *Modelling Simul. Mater. Sci. Eng.* 18 (2010), 015012
57. Friauf, R. J. Correlation Effects for Diffusion in Ionic Crystals. *J. Appl. Phys.* 1962, 33 (1), 494–505.
58. Wang, Y.; Richards, W. D.; Ong, S. P.; Miara, L. J.; Kim, J. C.; Mo, Y.; Ceder, G. Design Principles for Solid-State Lithium Superionic Conductors. *Nat. Mater.* 2015, 14 (10), 1026–1031.
59. Jand, S. P.; Zhang, Q.; Kaghazchi, P. Theoretical Study of Superionic Phase Transition in Li<sub>2</sub>S. *Sci. Rep.* 2017, 7 (1), 5873.

60. Altendorfer, F.; Bührer, W.; Anderson, I.; Schärpf, O.; Bill, H.; Carron, P. L.; Smith, H. G. Lithium Diffusion in the Superionic Conductor Li<sub>2</sub>S. *Phys. B Condens. Matter* 1992, **180–181** (92), 795–797.
61. He, X.; Zhu, Y.; Mo, Y. Origin of Fast Ion Diffusion in Super-Ionic Conductors. *Nat. Commun.* 2017, **8** (May), 1–7.
62. Weihang Xie, Zeyu Deng, Zhengyu Liu, Theodosios Famprakis, Keith T. Butler, and Pieremanuele Canepa, Effects of Grain Boundaries and Surfaces on Electronic and Mechanical Properties of Solid Electrolytes, *Adv. Energy Mater.* 2024, **14**, 2304230
63. Pieremanuele Canepa, James A. Dawson, Gopalakrishnan Sai Gautam, Joel M. Statham, Stephen C. Parker, and M. Saiful Islam, Particle Morphology and Lithium Segregation to Surfaces of the Li<sub>7</sub>La<sub>3</sub>Zr<sub>2</sub>O<sub>12</sub> Solid Electrolyte, *Chem. Mater.* 2018, **30**, 3019–3027.
64. Bo Gao, Randy Jalem, and Yoshitaka Tateyama, Surface-Dependent Stability of the Interface between Garnet Li<sub>7</sub>La<sub>3</sub>Zr<sub>2</sub>O<sub>12</sub> and the Li Metal in the All-Solid-State Battery from First-Principles Calculations, *ACS Appl. Mater. Interfaces* 2020, **12**, 16350–16358
65. Bora Karasulu, Steffen P. Emge, Matthias F. Groh, Clare P. Grey, and Andrew J. Morris, /Ga-Doped Li<sub>7</sub>La<sub>3</sub>Zr<sub>2</sub>O<sub>12</sub> Garnets as Li-Ion Solid-State Battery Electrolytes: Atomistic Insights into Local Coordination Environments and Their Influence on <sup>17</sup>O, <sup>27</sup>Al, and <sup>71</sup>Ga NMR Spectra, *J. Am. Chem. Soc.* 2020, **142**, 3132–3148
66. Juefan Wang, Abhishek A. Panchal, Gopalakrishnan Sai Gautam and Pieremanuele Canepa, The resistive nature of decomposing interfaces of solid electrolytes with alkali metal electrodes, *J. Mater. Chem. A*, 2022, **10**, 19732
67. Richard Tran, Zihan Xu, Balachandran Radhakrishnan, Donald Winston, Wenhao Sun, Kristin A. Persson & Shyue Ping Ong, Data Descriptor: Surface energies of elemental crystals, *Sci Data*, 2016, **3**, 160080
68. Ieuan David Seymour and Ainara Aguadero, Suppressing void formation in all-solid-state batteries: the role of interfacial adhesion on alkali metal vacancy transport, *J. Mater. Chem. A*, 2021, **9**, 19901–19913
69. N. D. Lepley, N. A. W. Holzwarth, and Yaojun A. Du, Structures, Li<sup>+</sup> mobilities, and interfacial properties of solid electrolytes Li<sub>3</sub>PS<sub>4</sub> and Li<sub>3</sub>PO<sub>4</sub> from first principles, *Phys. Rev. B* 2013, **88**, 104103
70. Iek-Heng Chu, Han Nguyen, Sunny Hy, Yuh-Chieh Lin, Zhenbin Wang, Zihan Xu, Zhi Deng, Ying Shirley Meng, and Shyue Ping Ong, Insights into the Performance Limits of the Li<sub>7</sub>P<sub>3</sub>S<sub>11</sub> Superionic Conductor: A Combined First-Principles and Experimental Study, *ACS Appl. Mater. Interfaces* 2016, **8**, 7843–7853
71. T.L. Einstein, 5 - Equilibrium Shape of Crystals, Editor(s): Tatau Nishinaga, *Handbook of Crystal Growth* (Second Edition), Elsevier, 2015, Pages 215-264
72. Salvador Miracle-Sole. Facet shapes in a Wulff crystal. *Mathematical Results in Statistical Mechanics*, Satellite Colloquium of STATPHYS 20, 1998, Marseille, France. pp.83-101
73. Naiara Letícia Marana, Silvia Casassa, Mauro Francesco Sgroi, Lorenzo Maschio, Fabrizio Silveri, Maddalena D’Amore, and Anna Maria Ferrari, Stability and Formation of the Li<sub>3</sub>PS<sub>4</sub>/Li, Li<sub>3</sub>PS<sub>4</sub>/Li<sub>2</sub>S, and Li<sub>2</sub>S/Li Interfaces: A Theoretical Study, *Langmuir* 2023, **39**, 18797–18806
74. N. D. Lepley and N. A. W. Holzwarth, Modeling interfaces between solids: Application to Li battery materials, *Phys. Rev. B* 2015, **92**, 214201

75. Luis E. Camacho-Forero, Perla B. Balbuena, Exploring interfacial stability of solid-state electrolytes at the lithium-metal anode surface, *Journal of Power Sources* 396 (2018) 782–790
76. Takanobu Yamada, Seitaro Ito, Ryo Omoda, Taku Watanabe, Yuichi Aihara, Marco Agostini, Ulderico Ulissi, Jusef Hassoun, and Bruno Scrosati, All Solid-State Lithium–Sulfur Battery Using a Glass-Type P<sub>2</sub>S<sub>5</sub>–Li<sub>2</sub>S Electrolyte: Benefits on Anode Kinetics, *Journal of The Electrochemical Society*, 162 (4) A646-A651 (2015)

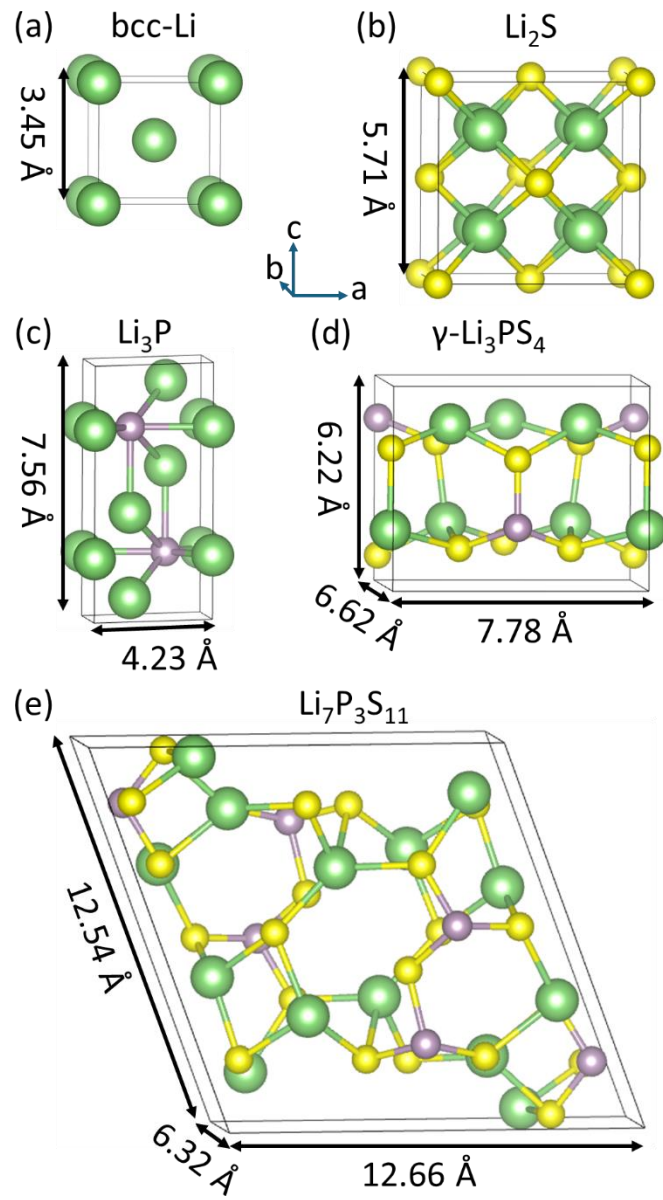
## Supporting Information

**Supporting Table S1.** Calculated chemical potentials from different sets of subsystems.

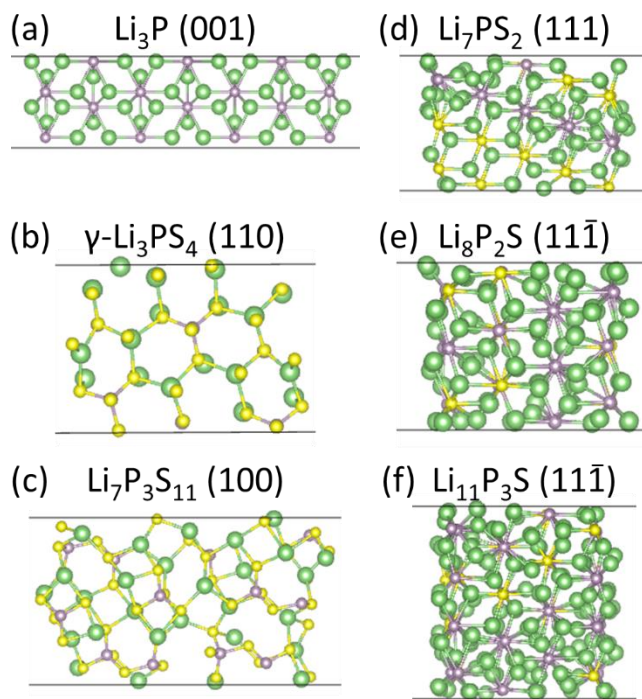
	$\mu_{\text{Li}}$ (eV)	$\mu_{\text{P}}$ (eV)	$\mu_{\text{S}}$ (eV)
Set 1: bcc-Li, Li <sub>2</sub> S, Li <sub>3</sub> P	-1.90	-8.23	-8.17
Set 2: Li <sub>2</sub> S, Li <sub>3</sub> P, P <sub>2</sub> S <sub>5</sub>	-3.44	-3.60	-5.09
Set 3: bcc-Li, bulk S, bulk P	-1.90	-5.38	-4.13

**Supporting Table S2.** Calculated formation energies per formula unit of the studied systems using the chemical potentials from Table S1.

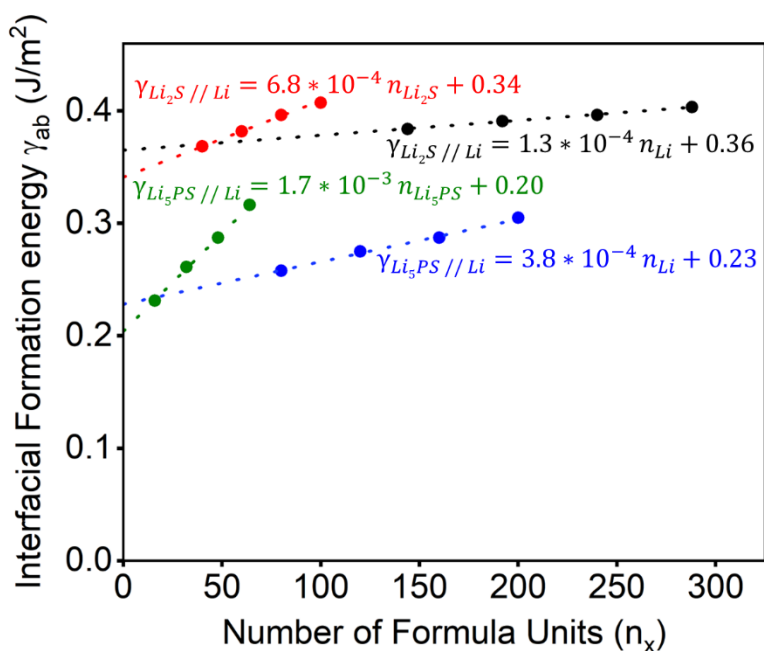
(eV)	Set 1	Set 2	Set 3
bcc-Li	0.0	1.54	0.0
Li <sub>3</sub> P	0.0	0.0	-0.71
$\gamma$ -Li <sub>3</sub> PS <sub>4</sub>	1.43	-0.11	-0.95
Li <sub>7</sub> P <sub>3</sub> S <sub>11</sub>	1.68	-0.09	-0.85
Li <sub>2</sub> S	0.0	0.0	-1.35
Li <sub>7</sub> PS <sub>2</sub>	0.04	0.04	-1.05
Li <sub>5</sub> PS	0.05	0.05	-0.93
Li <sub>8</sub> P <sub>2</sub> S	0.04	0.04	-0.85
Li <sub>11</sub> P <sub>3</sub> S	0.03	0.03	-0.81
P <sub>2</sub> S <sub>5</sub>	3.53	0.0	-0.17



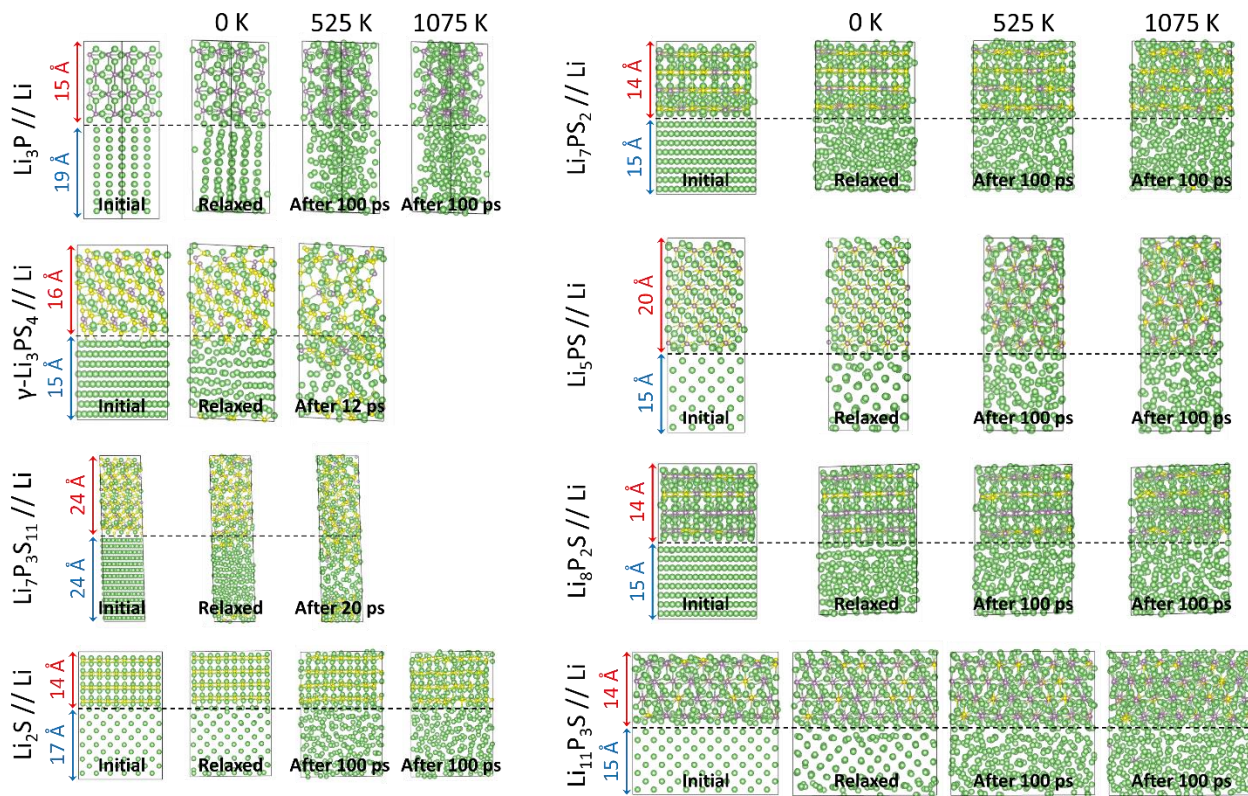
**Supporting Figure S1.** Unit cells for a) bcc-Li, b)  $\text{Li}_2\text{S}$ , c)  $\text{Li}_3\text{P}$ , d)  $\gamma\text{-Li}_3\text{PS}_4$ , and e)  $\text{Li}_7\text{P}_3\text{S}_{11}$ . Green, purple and yellow spheres represent Li, P and S atoms, respectively.



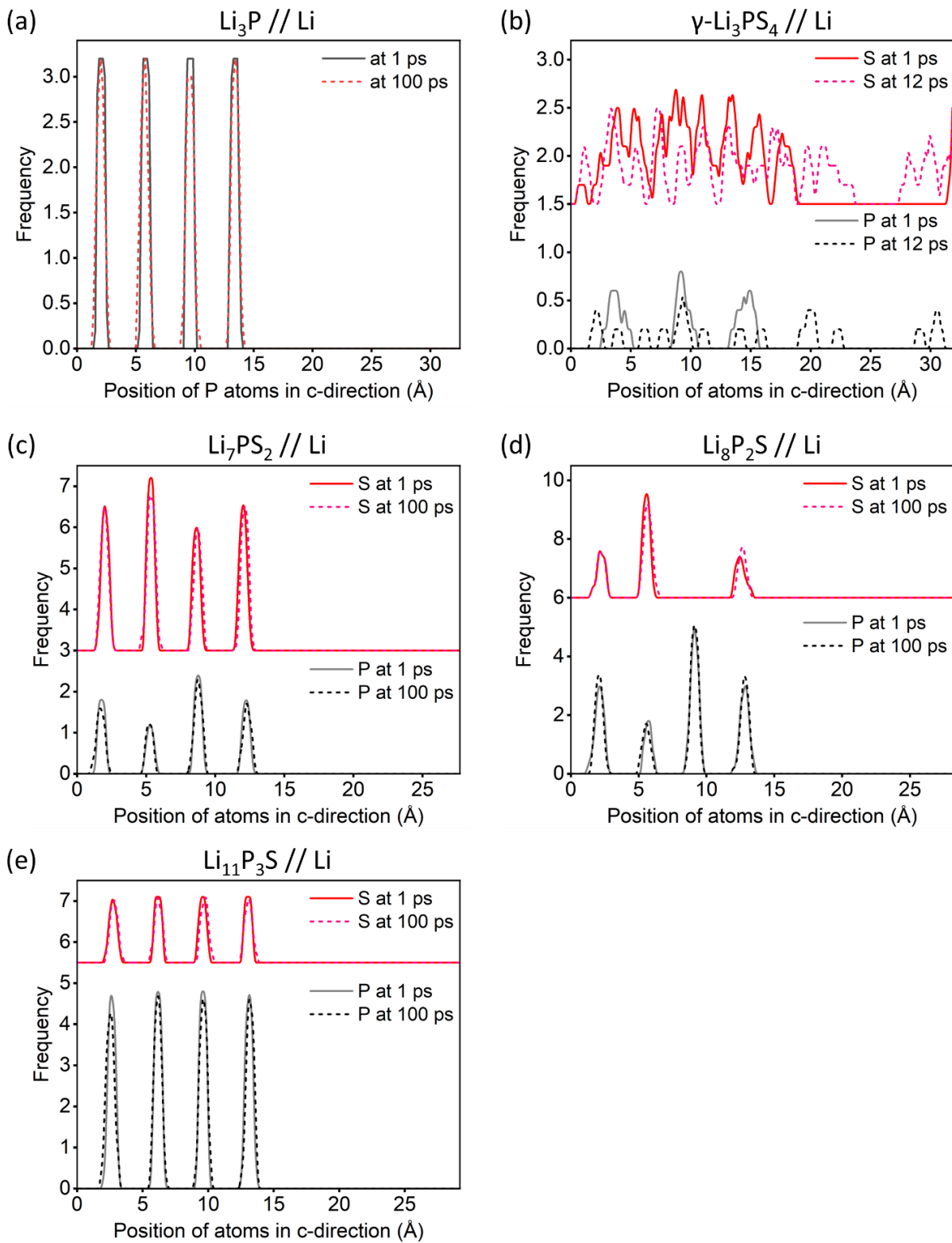
**Supporting Figure S2.** Energetically the most favourable surfaces. a)  $\text{Li}_3\text{P}$  (100), b)  $\gamma\text{-Li}_3\text{PS}_4$  (110), c)  $\text{Li}_7\text{P}_3\text{S}_{11}$  (100), d)  $\text{Li}_7\text{PS}_2$  (111), e)  $\text{Li}_8\text{P}_2\text{S}$  ( $11\bar{1}$ ), and f)  $\text{Li}_{11}\text{P}_3\text{S}$  ( $11\bar{1}$ ). Green, purple and yellow spheres represent Li, P and S atoms, respectively.



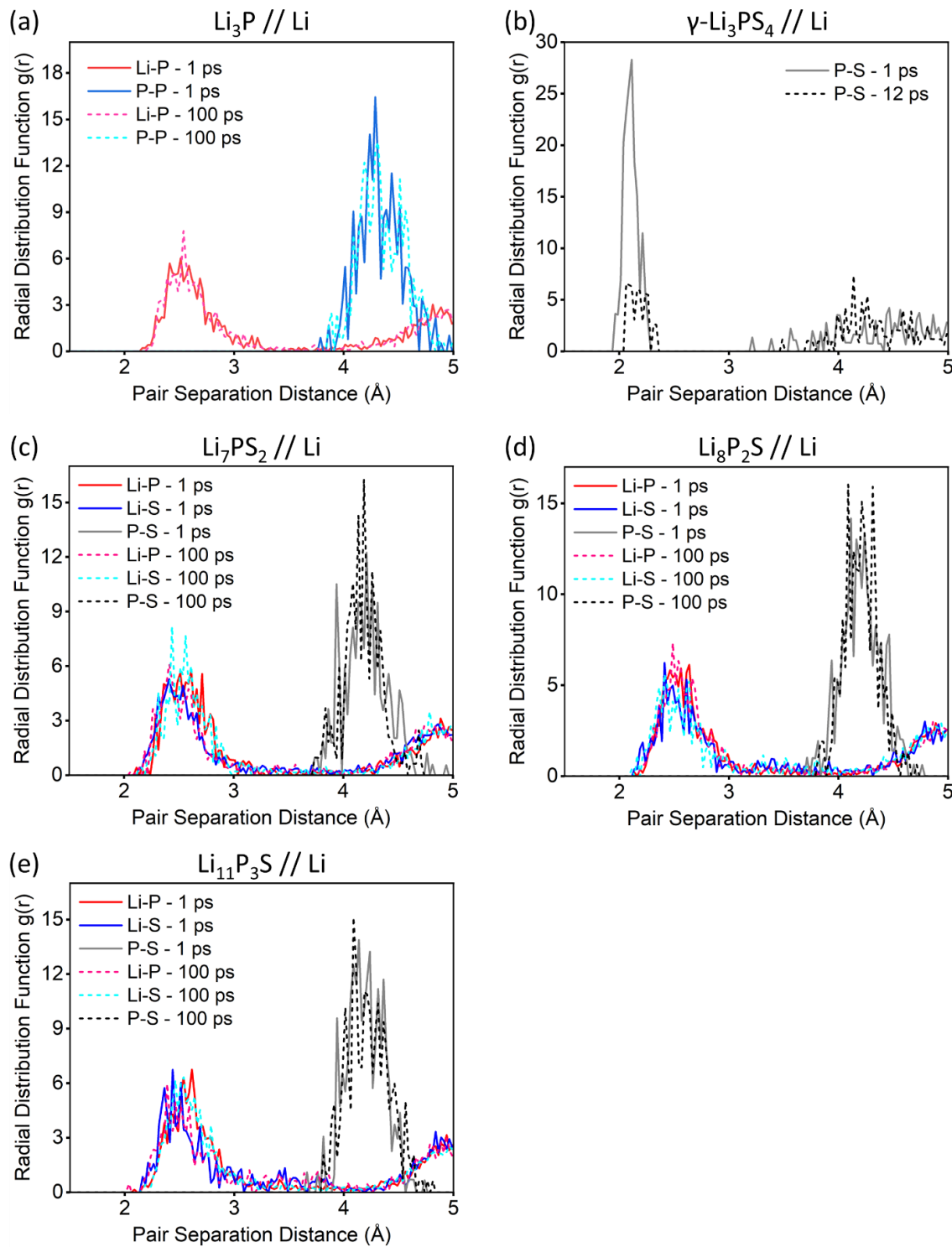
**Supporting Figure S3.** Linear dependence of the interface formation energy as a function of slab thickness for  $\text{Li}_2\text{S} // \text{Li}$  and  $\text{Li}_5\text{PS} // \text{Li}$  interface structures.



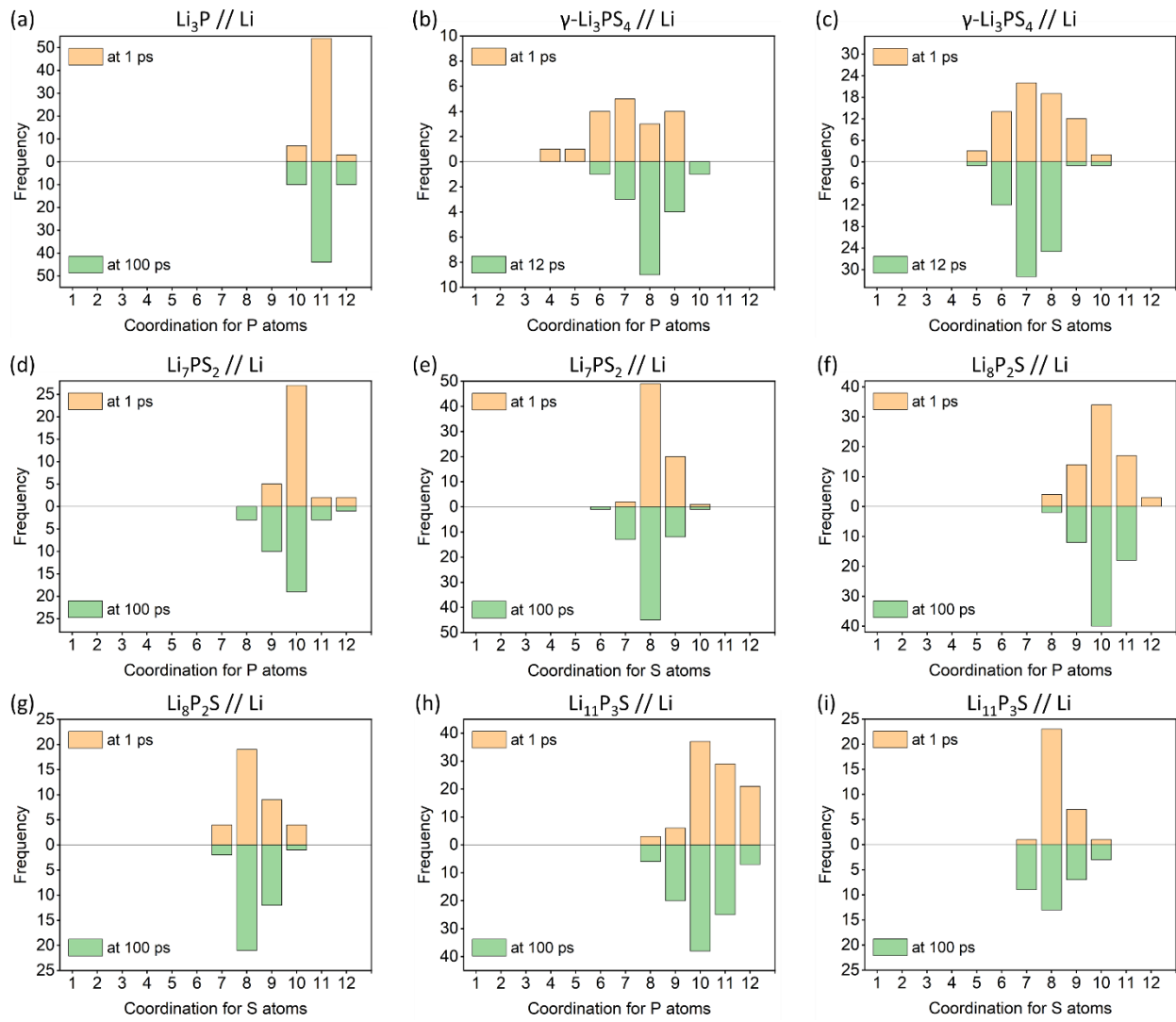
**Supporting Figure S4.** The evolution of studied interface structures. Initial (initially constructed structure by INTERFACER), Relaxed (fully DFT optimised structure – both lattice vectors and atomic positions – at 0 K) and After 100 ps (evolution of the structure during AIMD simulations at 525 K and 1075 K). The black dashed lines mark the initial position of the interface. Green, purple and yellow spheres represent Li, P and S atoms, respectively.



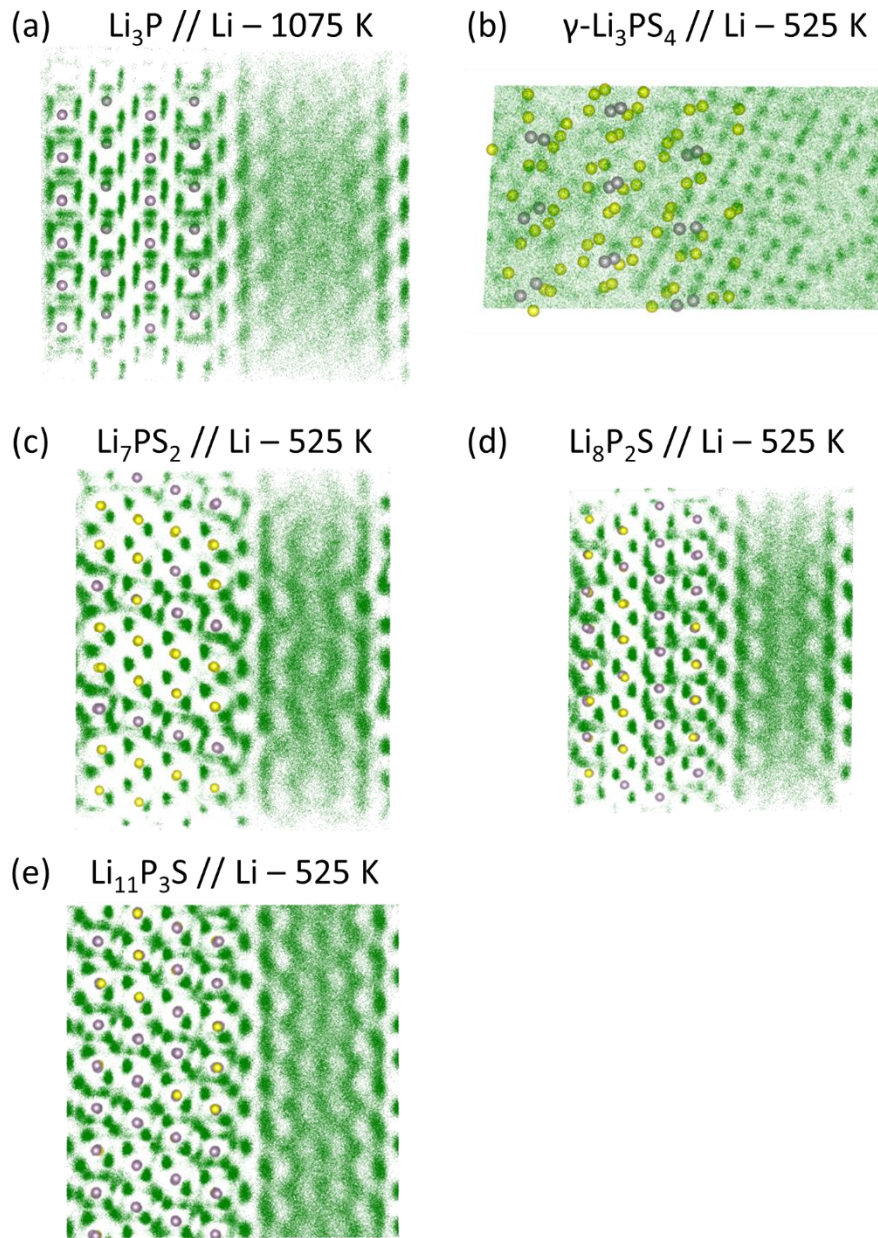
**Supporting Figure S5.** The positional histogram of P and S atoms along c-axis (perpendicular to the interface in a)  $\text{Li}_3\text{P} // \text{Li}$ , b)  $\gamma\text{-Li}_3\text{PS}_4 // \text{Li}$ , c)  $\text{Li}_7\text{PS}_2 // \text{Li}$ , d)  $\text{Li}_8\text{P}_2\text{S} // \text{Li}$ , and e)  $\text{Li}_{11}\text{P}_3\text{S} // \text{Li}$  at certain time steps during AIMD simulation at 525 K.



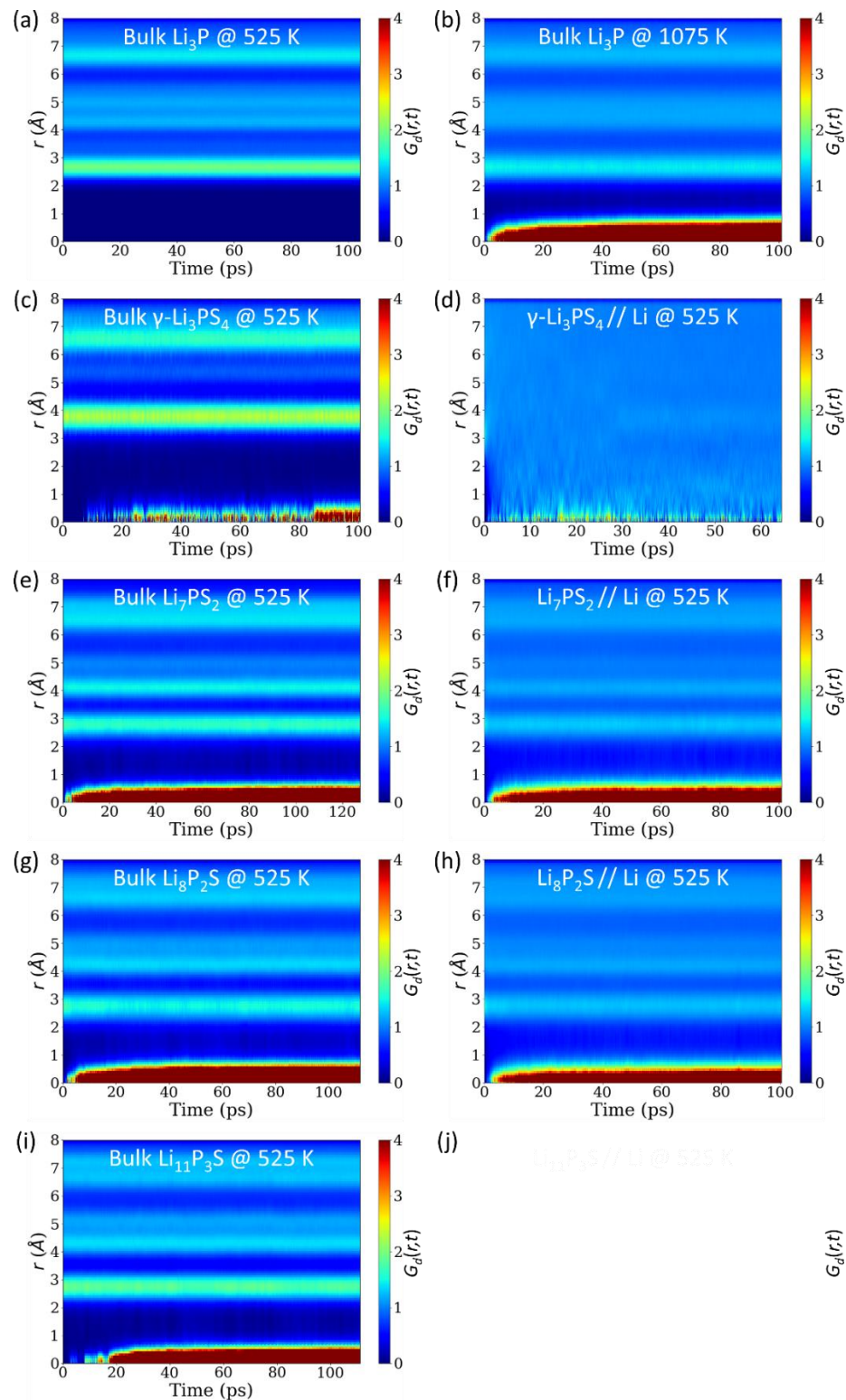
**Supporting Figure S6.** The radial distributions of certain atomic pairs in a)  $\text{Li}_3\text{P} // \text{Li}$ , b)  $\gamma\text{-Li}_3\text{PS}_4 // \text{Li}$ , c)  $\text{Li}_7\text{PS}_2 // \text{Li}$ , d)  $\text{Li}_8\text{P}_2\text{S} // \text{Li}$ , and e)  $\text{Li}_{11}\text{P}_3\text{S} // \text{Li}$  at certain time steps during AIMD simulation at 525 K.



**Supporting Figure S7.** The coordination numbers for a) P atoms in  $\text{Li}_3\text{P} // \text{Li}$ , b) P atoms in  $\gamma\text{-Li}_3\text{PS}_4 // \text{Li}$ , c) S atoms in  $\gamma\text{-Li}_3\text{PS}_4 // \text{Li}$ , d) P atoms in  $\text{Li}_7\text{PS}_2 // \text{Li}$ , e) S atoms in  $\text{Li}_7\text{PS}_2 // \text{Li}$ , f) P atoms in  $\text{Li}_8\text{P}_2\text{S} // \text{Li}$ , g) S atoms in  $\text{Li}_8\text{P}_2\text{S} // \text{Li}$ , i) P atoms in  $\text{Li}_{11}\text{P}_3\text{S} // \text{Li}$ , and i) S atoms in  $\text{Li}_{11}\text{P}_3\text{S} // \text{Li}$  at certain time steps during AIMD simulation at 525 K.



**Supporting Figure S8.**  $\text{Li}^+$ -ion trajectory (green) for a)  $\text{Li}_3\text{P} // \text{Li}$  at 1075 K, b)  $\gamma\text{-Li}_3\text{PS}_4 // \text{Li}$  at 525 K, c)  $\text{Li}_7\text{PS}_2 // \text{Li}$  at 525 K, d)  $\text{Li}_8\text{P}_2\text{S} // \text{Li}$  at 525 K, e)  $\text{Li}_{11}\text{P}_3\text{S} // \text{Li}$  at 525 K. The positions of the phosphorus (purple) and sulphur (yellow) atoms at time  $t = 0$  ps are shown in the background.



**Supporting Figure S9.** The distinct part of the Van Hove correlation function for Li atoms in a) bulk  $\text{Li}_3\text{P}$  at 525 K, b) bulk  $\text{Li}_3\text{P}$  at 1075 K, c) bulk  $\gamma\text{-Li}_3\text{PS}_4$  at 525 K, d)  $\gamma\text{-Li}_3\text{PS}_4/\text//\text{ Li}$  at 525 K, e)  $\text{Li}_7\text{PS}_2$  at 525 K, f)  $\text{Li}_7\text{PS}_2/\text//\text{ Li}$  at 525 K, g)  $\text{Li}_8\text{P}_2\text{S}$  at 525 K, h)  $\text{Li}_8\text{P}_2\text{S}/\text//\text{ Li}$  at 525 K, i)  $\text{Li}_{11}\text{P}_3\text{S}$  at 525 K and, j)  $\text{Li}_{11}\text{P}_3\text{S}/\text//\text{ Li}$  at 525 K.